

**A&A manuscript no.**  
 (will be inserted by hand later)  
**Your thesaurus codes are:**  
 4(10.11.1; 10.19.2; 10.19.3; 08.16.4)

**ASTRONOMY  
 AND  
 ASTROPHYSICS**

# Distribution functions for evolved stars in the inner galactic Plane

Maartje N. Sevenster<sup>1,3</sup>, Herwig Dejonghe<sup>2</sup>, Katrien Van Caelenberg<sup>2</sup> and Harm J. Habing<sup>1</sup>

<sup>1</sup> Sterrewacht Leiden, POBox 9513, 2300 RA Leiden, The Netherlands

<sup>2</sup> Sterrenkundig Observatorium, Krijgslaan 281, B-9000 Gent, Belgium

<sup>3</sup> Presently at MSSSO/RSAA, Private Bag Weston Creek PO, Weston ACT 2611, Australia

Received ; accepted

**Abstract.** We present dynamical distribution functions for a homogeneous sample of oxygen-rich, evolved, intermediate-mass stars in the inner galactic plane. We use an axisymmetric, two-component Stäckel potential that satisfies recent constraints on the galactic potential, amongst others a slightly declining local rotation curve. We show that this potential is adequate to model stellar-kinematic samples with radial extent ranging from  $\sim 100$  pc to  $\sim 5$  kpc in the Galaxy.

The stable two-integral model that gives the best fit to the first three projected moments provides a very good global representation of the data but fails to reproduce the central line-of-sight dispersion, the central apparent scaleheight and the almost-cylindrical rotation at intermediate longitudes ( $5^\circ < |\ell| < 15^\circ$ ). All these features, indicative of the galactic Bar, are fitted well by a three-integral model. We discuss various properties of the two- and three-integral distribution functions and the implications for galactic structure. A somewhat thicker disk component is needed to explain the observed distribution of older AGB stars in the plane; this component at the same time fits the kinematics of AGB stars at higher latitudes better than the thinner disk. We find that the Disk and the Bulge, as traced by AGB stars, are very similar dynamically and could well be one and the same component. There is a dynamically distinct component in the inner 100 pc of the Bulge, however.

## 1. Introduction

Methods to analyse observational data almost always fall into one of two classes, “direct” and “indirect” methods. The former seek to derive (deproject) the desired quantities in a direct manner from the observed quantities, the latter to predict the observables from a purely theoretical model and then accept or reject the model by comparing the predictions to the observations.

In the field of modelling galactic stellar dynamics, two types of indirect methods prevail. One is to construct models via N-body simulation (eg. Fux 1997), the other via the (semi-direct) Schwarzschild method (Schwarzschild 1979, eg. Zhao 1996). In this paper we will use an indirect, Schwarzschild-type method to model the stellar dynamics of the inner Milky Way Galaxy. We test assumed dynamical distribution functions for their ability to reproduce the distribution of our sample of evolved, intermediate-mass stars (Sevenster et al. 1997a,b, S97A,S97B). This sample is representative of a large fraction of the stellar content of the Galaxy, but does not sample the old, spherical Bulge or the Halo. Therefore, it is justified to consider its dynamical distribution in a global, fixed potential, unlike most Schwarzschild models. Rather than trying to build self-consistent models from an unsuitable sample, we constrain the model gravitational potential with a variety of other recent observations. The goal is to find the dynamical characteristics of the inner Galaxy and whether there are clearly distinct dynamical components.

In Sect. 2 and Sect. 3 we describe the method and its detailed implementation, in particular the choice of the potential. In Sect. 4 we discuss the resulting two-integral model and its errors and stability. We present a three-integral model in Sect. 5 and a two-integral model for a galactic-centre sample in Sect. 6. We interpret the results in Sect. 7 and we end with conclusions in Sect. 8.

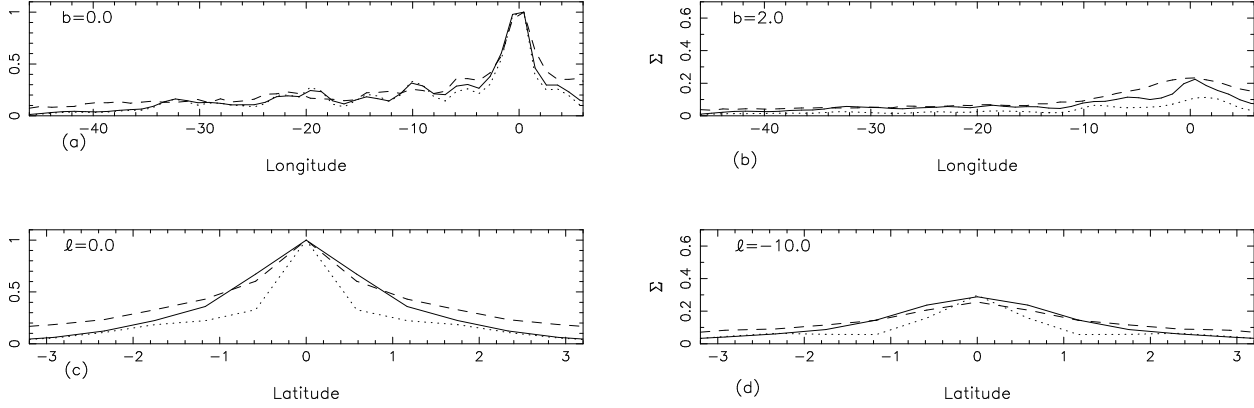


**Fig. 1.** Cuts in longitude and latitude through the OH/IR data smoothed with round kernels (initial kernel  $1^\circ$ , solid), smoothed with elongated kernels (initial kernel  $1^\circ$  in  $\ell$  and  $0.5^\circ$  in  $b$ , dotted) and the COBE-DIRBE surface-density map (dashed). All densities are normalized separately to have a peak density of 1 and interpolated onto a grid of  $(1^\circ, 0.67^\circ)$ .

## 2. Method

The distribution function of a stellar system is a function of at most three isolating integrals of motion  $I_i$ , according to Jeans' theorems. It gives the density of stars in the full six-dimensional phase-space  $(\mathbf{x}, \mathbf{V})$ . Integrating over all velocities, we get the true  $n^{\text{th}}$ -order moments  $M^{(n)}$  of the distribution function according to :

$$M^{(n)} \equiv \rho \langle \left( \prod_{k=1}^n V_k \right) \rangle = \int \left( \prod_{k=1}^n V_k \right) f(\mathbf{I}) d^3 \mathbf{V} \quad n = 0, 1, \dots \quad V_k \in (V_x, V_y, V_z) \quad 1$$

leaving out the dependencies on  $(\mathbf{x})$ . There are one zeroth-order moment ( $M^{(0)}$ ), three first-order moments ( $M^{(1)}$ ), nine second-order moments ( $M^{(2)}$ ) (six of which are independent) and so on. The method we use to model the distribution function of a galactic stellar sample was developed by Dejonghe (1989). For details we refer to that article; here we discuss the method only briefly. In a given gravitational potential, a distribution function is built from a library of orbital components that are (analytic) functions of the integrals of motion in that potential. By minimizing the quadratic differences  $D$  between moments of the model distribution ( $M_M$ ) and the observed distribution ( $M_O$ ),

$$D \equiv \sum_{\text{sky}} \left[ \left( w_0 (M_O^{(0)} - M_M^{(0)}) / M_M^{(0)} \right)^2 + \left( w_1 (M_O^{(1)} - M_M^{(1)}) / M_M^{(1)} \right)^2 + \left( w_2 (M_O^{(2)} - M_M^{(2)}) / M_M^{(2)} \right)^2 + \dots \right], \quad 2$$

it determines, sequentially, the best combination of components and the corresponding coefficients. The moments can have different weights  $w_i$  in the determination of  $D$  according to the importance they should have in the fit. Because of its quadratic-programming character we will use “QP” to refer to the modelling program. There is no true  $\chi^2$  connected to the fit, because there is no optimization of free parameters in the strict sense: the parameter  $D$  can be used only to compare the goodness of fit between models with the same potential and input data. To compare different potentials or data sets, the ratio of the initial to the converged value of  $D$  might be used.

## 3. Implementation

In this paper, we use QP with an axisymmetric potential. The Galaxy's density distribution is not axisymmetric, but the probably small eccentricity of the potential and the not too-strongly barlike inner stellar kinematics (see Sevenster 1999) indicate that the non-axisymmetric part of the potential is negligible in a first approach. The influence of the third integral is not negligible, in any case not for the galactic Disk (eg. Oort 1965). After starting our investigations with two-integral (2I) models, that are easier to interpret, we construct a three-integral (3I) axisymmetric model to try and overcome the limitations of the 2I model.

In the models presented in this paper, we include the first three projected moments of distribution functions in the fit. The moments used for the comparison between model distribution function and observations are hence  $\Sigma$  (the surface-number density),  $\Sigma \langle V_{\text{los}} \rangle$  and  $\Sigma \langle V_{\text{los}}^2 \rangle$ . The weights  $w_i$  in Eq. 2 are all equal to 1 in the models presented in this paper. In the figures we will mostly show the more commonly-used derived moments  $\Sigma$ ,  $\langle V_{\text{los}} \rangle$  and  $\sigma_{\text{los}}$ .

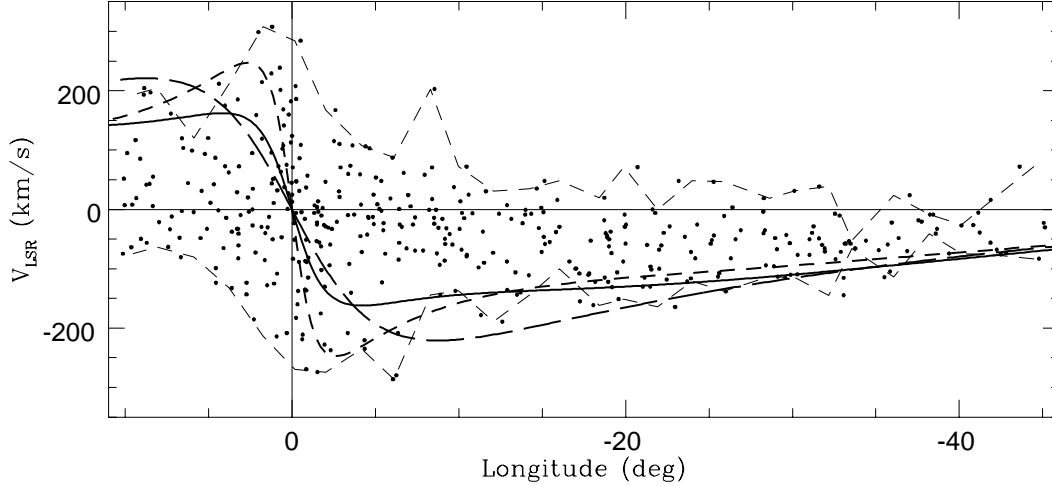


**Fig. 2.** The longitude–velocity diagram for the OH/IR stars with the rotation curves for the BD2 (long-dashed), the HI2 (short-dashed) and the AX2 (solid) potentials (see Sect. 3.2, Table 2). The thin dashed lines connect the maximum and minimum observed velocities, respectively, in longitude bins. stellar velocities. The BD2 potential yields too high velocities at intermediate longitudes; since stars have dispersions the rotation curve should fall in general somewhat below the maximum observed stellar line-of-sight velocities, as is the case for the AX2 and HI2 potentials.

**Table 1.** Average dispersions in coordinate separations.

$N_{\text{nn}}$	$\ell$	$b$	$V$
	$^{\circ}$	$^{\circ}$	km/s
10	0.8	0.8	135
20	1.1	1.1	135
30	1.5	1.3	135
50	2.2	1.5	135

### 3.1. Data

The data were acquired specifically to constrain optimally dynamical models of the galactic Plane (S97A, S97B). The sample consists of positions on the sky (accuracy  $\sim 0''.5$ ) and line-of-sight velocities (accuracy  $\sim 1 \text{ km s}^{-1}$ ) with respect to the local standard of rest (LSR) of OH/IR stars; oxygen-rich, asymptotic-giant-branch (AGB) stars in the thermally-pulsing phase. These stars form a partly relaxed population (0.5–7.5 Gyr, Sevenster 1999) and trace the dominant mass distribution (Frogel 1988). The region covered in galactic coordinates is  $-45^\circ < \ell < 10^\circ$  and  $|b| < 3^\circ$ . In total 507 objects were found, forming the AOSP (Australia telescope Ohir Survey of the Plane) sample used in this paper. The QP program will correct the velocities for the motion of the LSR, assuming the LSR is on a circular orbit at  $R_\odot \equiv 8 \text{ kpc}$  in the *model* potential.

In Table 1 we give the dispersions, using all stars in the sample, in the distribution of separations in all three coordinates for different numbers of nearest neighbours  $N_{\text{nn}}$  (on the sky). The average velocity difference between stars does not change with number of nearest neighbours. Since the velocity profile sampled by the stars has to change with position on the sky, this means that the velocities of neighbouring stars are completely independent. Therefore, we use adaptive-kernel smoothing to grid the data on the sky (Merritt & Tremblay 1994), but treat the velocity coordinate separately (cf. their equation 40).

**Table 2.** Potential models.  $R_\odot \equiv 8$  kpc. This table is discussed in Sect. 3.2.

Name	$M_{\text{tot}}$ $M_\odot$	$A$ $t'$	$B$ $t'$	$V_{\text{LSR}}$ km/s	$2AR_\odot$ km/s	$dV/dR$ $t'$	$\rho_\odot$ $M_\odot/\text{pc}^3$	$\Sigma_\odot$ $M_\odot/\text{pc}^2$	$\kappa_\odot$ $t'$	$q_{\text{halo}}$	$q_{\text{d,b}}$ %	$f_{\text{d,b}}$ %	$\Delta^2$ $\text{kpc}^2$
<b>AX2</b>	1.8E11	15.5	-11.7	217	248	-3.8	0.01	20	36	1.006	2.5, -	5, -	0.1
<b>BD2</b>	4.0E11	13.6	-14.4	224	218	+0.75	0.05	43	40	1.01	50, -	10, -	1.0
<b>HI2</b>	2.8E11	14.3	-14.5	230	229	+0.13	0.02	32	41	1.002	20, -	4, -	.07
<b>HI3</b>	2.5E11	14.1	-13.6	221	226	-0.63	0.01	28	39	1.03	15, 2.5	5, 1	0.1
<b>AX3</b>	4.0E11	12.4	-14.8	217	198	+2.4	0.02	32	40	1.01	10, 2.5	1, 10	.07

$t' = \text{km/s/kpc}$

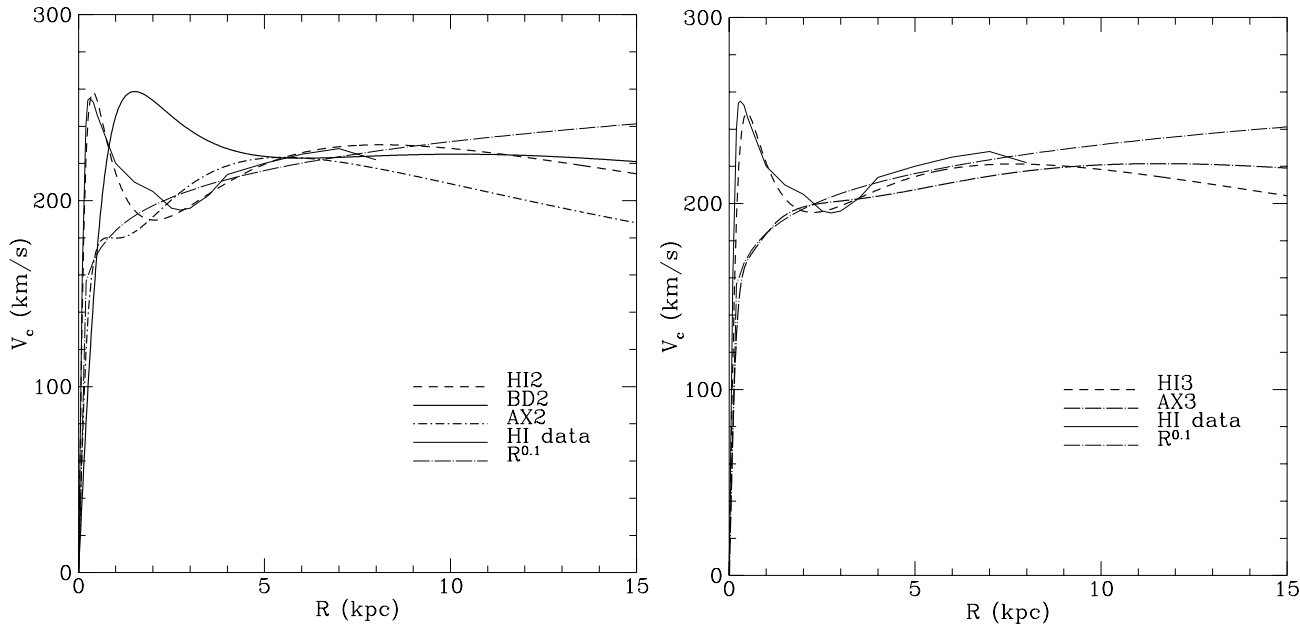


**Fig. 3.** Circular-velocity curves for various model potentials and as derived from observations. In both panels the thin lines indicate observed rotation curves, derived from HI data (solid, Burton & Gordon 1978) and from the stellar surface brightness (dot-dashed,  $v_c = 184 \text{ km s}^{-1} R_{\text{kpc}}^{0.1}$  Allen et al. 1983). The thick curves are the fitted potentials. **a** Two-component Stäckel KK-model potentials fitted to HI (HI2, dashed), to the stellar surface brightness in the inner regions (AX2, dot-dashed) and to constant circular velocity outside 5 kpc (BD2, Batsleer & Dejonghe 1994). **b** Three-component Stäckel KK-model potentials fitted to HI (HI3, dashed) and to the stellar surface brightness (AX3, dot-dashed).

First, the data are smoothed with initial gaussian kernels of  $1^\circ \times 1^\circ \times 30 \text{ km s}^{-1}$ . (These initial-kernel sizes were optimized to retain the scales of the large-scale distribution without showing individual stars, cf. Table 1.) Then, for each star, the spatial kernel is adapted according to the surface density and the mean velocity and velocity dispersion are determined from the velocity profile thus created at its position on the sky (so, the ratio of the spatial-kernel sizes was kept constant). Finally, the surface density, mean velocity and velocity dispersion are calculated on a regular grid, still using gaussian distributions in all three dimensions, with these final parameters.

In Fig. 1a-d we compare the resulting surface density with that of the COBE-DIRBE observations (Dwek et al. 1995). In the same figure, we show the surface density resulting from smoothing the data with elongated kernels, to reflect the possible difference between the vertical and the radial density scale. The COBE- and the AOSP surface densities clearly trace a similar population (the evolved late-type stars) and The round kernels provide slightly better agreement with the COBE data and are also favoured by the results give in Table 1. We thus use the round-kernel surface density for our standard model, but also give results for the elongated-kernel surface density.

**Table 3.** Observed values for the potential parameters (units as in Table 2).

Quantity	Value (ref)	Value (ref)	Value (ref)	Value (ref)	References
$A$	$14.4 \pm 1.2$ (1)	$11.3 \pm 1.3$ (2)	$19 \pm 6$ (3)	$14.82 \pm 0.84$ (9)	1 Kerr & Lynden-Bell 1986
$B$	$-12.0 \pm 2.8$ (1)	$-13.9 \pm 0.9$ (2)	$-13 \pm 5$ (3)	$-12.37 \pm 0.64$ (9)	2 Hanson 1987
$V_{\text{LSR}}$	184 (4)	$200 \pm 10$ (10)	$231 \pm 21$ (9)		3 Evans & Irwin 1995
$2AR_{\odot}$	228 (5)	248 (6)	257 (7)	252 (9)	4 Rohlfs et al. 1986
$dV/dR$	$-3.7$ (4)	$-2.4$ (9)			5 Caldwell & Coulson 1989
$\rho_{\odot}$	0.1 (8)	$0.076 \pm 0.015$ (11)			6 Schechter et al. 1989
$\kappa_{\odot}$	36 (1)				7 Pont et al. 1994
$\Sigma_{\odot}$	46 $\pm 9$ (12)				8 Kuijken & Gilmore 1989b
$M_{50\text{kpc}}$	$4.9 \pm 1.1 \cdot 10^{11}$ (13)				9 Feast & Whitelock 1997
					10 Merrifield 1992
					11 Creze et al. 1998
					12 Kuijken & Gilmore 1989a
					13 Kochanek 1996

### 3.2. Potential

To model the galactic potential, we use so-called Stäckel (S) potentials (see de Zeeuw 1985), because for those three integrals of motion are known analytically. The specific form of the S-potentials used in this work is that of a multiple, axisymmetric Kuzmin–Kutuzov (KK) potential (see Dejonghe & de Zeeuw 1988). The Galaxy is thus simulated by a small number of separate, axisymmetric components with different flattenings, but the same focal lengths to keep the over-all potential in Stäckel form, ie. separable in ellipsoidal coordinates. Batsleer & Dejonghe (1994) give values for the parameters that optimize the fit of a double S-KK potential to the large-scale rotation curve of the Galaxy, with the two components representing a (dark) halo and a disk (BD2, Table 2).

In Fig. 2, we show the longitude–velocity diagram of the AOSP sample, together with the rotation curves for the two-component potentials from Table 2. The BD2 potential has little mass in the central regions of the Galaxy; the rotation curve is shallower than the  $R^{0.1}$  curve determined for the inner Galaxy (Allen et al. 1983; see Fig. 3 and the AX2 potential in Fig. 2). The circular velocity at intermediate longitudes ( $10^{\circ}$  to  $20^{\circ}$ ) is too high; the extreme stellar velocities should be somewhat larger than the circular velocity, give or take statistical fluctuations, because the line-of-sight dispersion is larger than the asymmetric drift ( $\sim \sigma_R^2/120 \text{ km s}^{-1}$  in the Disk). In test runs we found that these short-comings inhibit the construction of realistic models for the AOSP sample, that is dominated by the Bulge potential. We therefore tried to find an S-KK potential that has more mass in the central regions, yields a realistic rotation curve and gives acceptable values for important parameters such as the local circular velocity and the Oort constants.

In Table 2, we list the values for these parameters for three double and two triple S-KK potentials. These potentials were constructed to fit various rotation curves for the Galaxy (Fig. 3). The columns in Table 2 give the total mass of the Galaxy  $M_{\text{tot}}$ , Oort's constants  $A$  and  $B$ , the local circular velocity  $V_{\text{LSR}}$ , the common combination  $2AR_{\odot}$ , the first radial derivative of the circular velocity  $dV/dR$  ( $R_{\odot} dV/dR = V_{\text{LSR}} - 2AR_{\odot}$ ), the local density  $\rho_{\odot}$ , surface density  $\Sigma_{\odot}$  and local epicyclic frequency  $\kappa_{\odot}$ , the flattening of the halo  $q_{\text{halo}}$ , the flattening of the second (third) component  $q_{\text{d,b}}$ , the fraction of the mass in the second (third) component  $f_{\text{d,b}}$  and the square of the “focal length”  $\Delta^2$ . For all details on these S-KK potentials and the parameters see Batsleer & Dejonghe (1994).

In Table 3 we list observed values for some of the quantities in Table 2, determined by various authors. The total mass of the Galaxy, the mass fractions of the Disk and Bulge and the flattenings of the components are not well established observationally and treated as mere parameters for the potentials rather than physical quantities. Even for the double KK potentials there is considerable freedom to create rotation curves of all sorts and at the same time obtain very realistic values for the important parameters. HI2 and HI3 are based on the assumption that the HI gas follows purely circular orbits, which is probably not the case in the inner Galaxy. They are therefore not likely to be realistic, but it is interesting that the HI-rotation curve as well as local parameters can be reproduced with so simple a potential.

An obvious limitation is that  $\Delta$  has to be the same for all components, in order to keep the total potential in Stäckel form. This means that all components simultaneously become more compact when increasing the contribution of the inner regions of the Galaxy. Therefore, all five potentials listed in Table 2 give quite acceptable values for all observational constants except  $\rho_{\odot}$ . Accordingly, the vertical forces at larger radii ( $R \sim R_{\odot}$ ) are not in agreement with observations (eg. Kuijken & Gilmore 1989a). Related results should be viewed with care; we will give most attention to

the inner Galaxy,  $R \lesssim 5$  kpc, where the potential is realistic and also the observations sample the distribution optimally (Fig. 5)

We will use the potential AX2, for which we deem the rotation curve most realistic. Its kinematic parameters, especially  $\kappa_\odot$ ,  $V_{\text{LSR}}$ ,  $2AR_\odot$ ,  $dV/dR$  and  $B$ , are best in agreement with observations. AX2 does not have a constant outer rotation curve, consistent with recent claims (Rohlfs et al. 1986; Binney & Dehnen 1997; Feast & Whitelock 1997; Honma & Sofue 1997). The self-consistent density for the AX2 potential is positive everywhere. Its central scalelength (200 pc) and scaleheight (120 pc) are of the order of those found for the density distribution of the AOSP sample (Sevenster 1999).

### 3.3. Two-integral orbital components

We use two families of 2I orbital components – full distribution functions in themselves – to build the total distribution function; the first has infinite extent (“bulge-like”), the second is limited in the vertical direction (“disky”). Their functional forms are:

$$F1(\alpha, \beta, i_s) = E^\alpha (EL_z^2/2)^\beta \quad \text{for } i_s L_z \geq 0 \text{ and } F1 = 0 \text{ otherwise ,} \quad 3$$

$$F2(\alpha, \beta, \gamma, z_0, i_s) = S^\alpha (2SL_z^2)^\beta [(E - S)/(S_0 - S)]^\gamma \quad \text{for } i_s L_z \geq 0 \text{ and } F2 = 0 \text{ otherwise,} \quad 4$$

with  $E$  the total energy and  $L_z$  the angular momentum, the two classical integrals in axisymmetric systems.  $S$  is the energy of an orbit that reaches just to  $z_0$  out of the plane and  $S_0$  the energy of a circular orbit in the plane, both for a given  $L_z$ . We will discuss the properties of F1 and F2 briefly and refer to Batsleer & Dejonghe (1995) for a thorough treatment of components of these types. The F1 and F2 components are all even in  $L_z$ ; to get rotation, the parameter  $i_s$  is introduced. If  $i_s = -1$  only the co-rotating half of phase space is populated, for  $i_s = 1$  only the counter-rotating half and for  $i_s = 0$  the full possible range of angular momenta is populated. Components with  $i_s = 0$  are therefore non-rotating. An impression of the appearance of those families of components can be obtained by considering their parameters one by one. The parameter  $\alpha$  indicates the degree of central concentration and  $\beta$  the degree of rotation in both families. For non-zero  $\beta$ , the density distributions become toroidal. For the second family (F2)  $z_0$  is the absolute vertical cut-off for the component and  $\gamma$  determines the vertical scaleheight. The larger  $\gamma$ , the faster the density falls off with increasing height above the plane. A smooth transition for  $\rho \rightarrow 0$  at  $z_0$  for all  $R$  is ensured by the functional form of the second family.

The program QP reads the allowed values for all parameters from an input library. For each component it determines the coefficient  $C$  for which the value of  $D$  (Eq. 2) is minimized. The component with smallest  $D$  is then chosen as the first in the series that forms the total distribution function. Subsequently, all the remaining components are checked for the smallest value of  $D$  in combination with the first component. The coefficient of the first component does not have to remain fixed; it can even become zero in the process of converging. The sum of the first  $N$  components has to be positive for all  $N$ , so that the series gives a valid distribution function - positive everywhere in phase space - at any instant in the convergence, but individual  $C$ 's can be negative in principle. In fact, one may use the negative coefficients to test if the model components have any physical meaning; when positive coefficients alternate with negative ones in successive components, the model is similar to a power-series development and thus a purely mathematic construct. This means that none of the components individually match the data well and one may want to consider a new component library. We demand that all coefficients be positive for all our models, but test the final library allowing also negative coefficients.

The best solution, for given input library, is reached when the value of  $D$  (Eq. 2) has converged to within a few percent. The number of components in the converged solution is mostly of the order of  $M_c = 5$  for the models in this paper. We ran QP with a great variety of input libraries, starting with one that spans a wide range for the parameters and fine tuning toward preferred solutions. For example, if  $\alpha = 20$  is selected from a library with  $\alpha = (3, 10, 20, 30)$  then the next library will have  $\alpha = (15, 20, 25)$ . These libraries are relatively small, with  $N_c \sim 60$  components, to reduce the computing time ( $t \propto N_c!/(N_c - M_c)!$ ). One should be careful not to exclude non-preferred values for the parameters once and for all, because QP seeks out the best *combination* of components. It may be that in the first trial runs, for example, F2 components with  $\alpha > 10$  are never used. After the fine-tuning process, such components could nevertheless improve the solution when combined with the final components. We therefore always ran QP with a large library ( $N_c \sim 250$ ), that combined the best library with earlier ones, as a final test. Mostly, the solution in these final runs did not differ from that obtained with the best (small) library.

In Fig. 4 we show how orbits populate different regions of phase space. The energies and angular momenta that an orbit can have are determined by the potential. A detailed explanation is given in the figure caption.

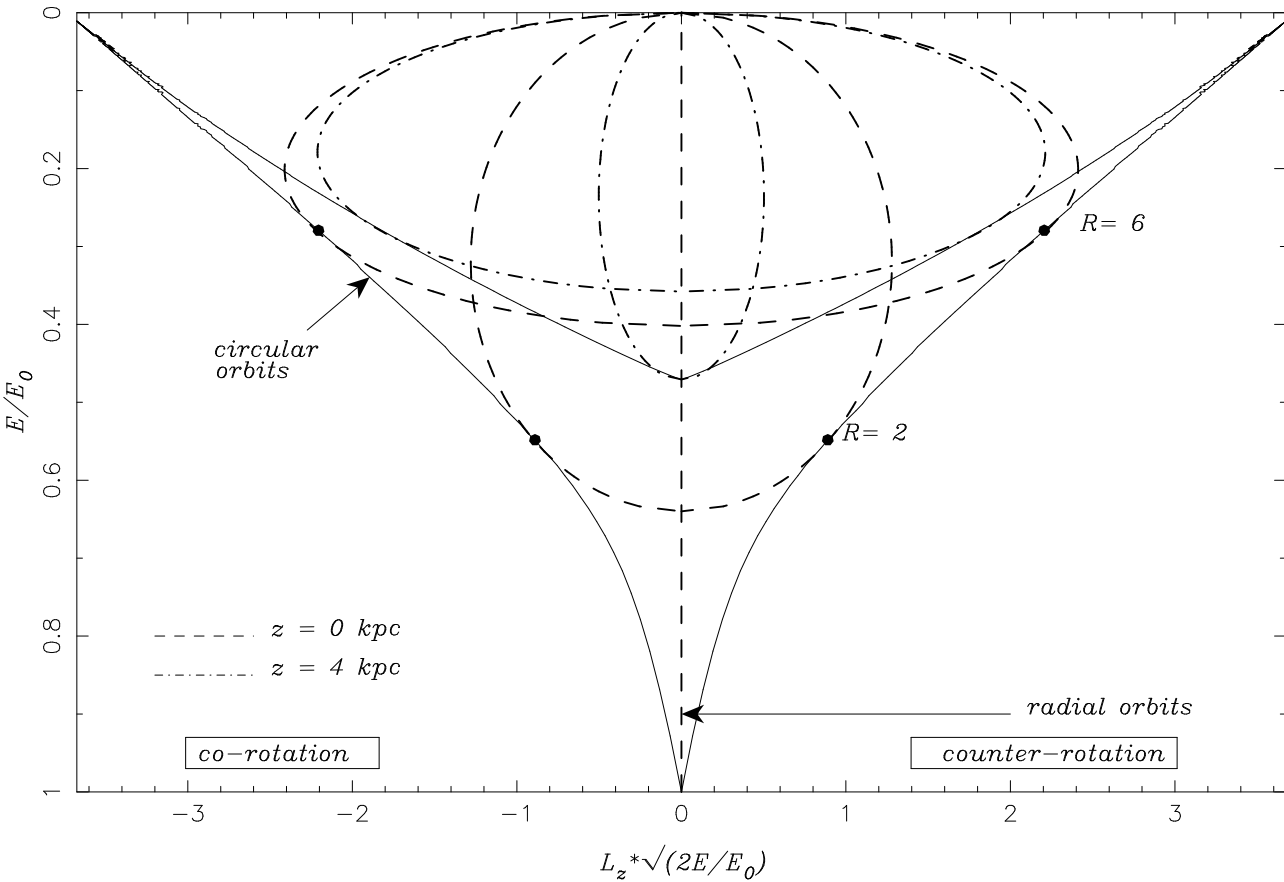


**Fig. 4.** Orbits are points in the  $(E, L_z)$  or phase space. For the AX2 potential they are arranged as follows. By convention, co-rotating orbits have negative angular momentum. The outer thin line indicates the  $(E, L_z)$  for circular orbits; the shape is determined by the potential and thus only valid for AX2. Only the regions inside this line can be populated, as circular orbits have maximum  $L_z$  for given  $E$ . The dashed ellipses are the perimeters of regions accessible for orbits that pass through the plane at a given radius  $R$ ; their intersections with the circular-orbit line obviously indicates the  $E, L_z$  of the circular orbit at  $R$ . The dot-dashed ellipses are the perimeters of regions accessible for orbits that pass through the  $z = 4$  kpc plane at given radius  $R$  (same  $R$ 's as for  $z = 0$  kpc). The thin line reminiscent of the circular-orbit line connects the maximum  $L_z$  for orbits with different  $E$ , that reach  $z = 4$  kpc somewhere along its orbit. For  $L_z = 0$ , the orbits are radial (vertical dashed line). Isotropic distributions ( $\beta = 0$ ) are independent of  $L_z$  and will give horizontal contours in this diagram. Rotating, disk-like distributions yield contours roughly parallel to co- and/or counter-rotating half of the circular-orbit line. If the distribution is flattened, say  $z < 4$  kpc, the phase-space density will only be non-zero between the two thin, solid lines (for maximum angular-momentum at  $z = 0$  and  $z = 4$ , respectively).  $L_z$  is scaled to increase the relative resolution in the inner regions ( $E \sim 1, L_z \sim 0$ ).

The components are integrated out to a predefined limit. For the models using the whole AOSP sample we use a horizon at 13 kpc; in every direction the model is integrated out to 13 kpc from the position of the observer (Fig. 5). This limit is chosen somewhat larger than the observational limit (Sevenster 1999). All galactic radii smaller than 5 kpc are thus sampled twice at each line of sight at  $|\ell| < 39^\circ$  and best constrained; radii between 6 kpc and 8 kpc are sampled at once or twice per line of sight (Fig. 5). Radii larger than 8 kpc are sampled only once for lines of sight at  $|\ell| > 36^\circ$ . At the largest longitude used in the modelling,  $45^\circ$ , the horizon lies at a galactic radius 9.2 kpc. In models for only low-outflow sources we use a horizon at 11 kpc, as these have a smaller observation limit (Sevenster 1999).

#### 4. Results

The best 2I distribution function (DFA) was obtained using the component library given in Table 4. Table 5 gives the components of DFA with their coefficients,  $C$ , as well as the masses,  $M_w$ , of the components in the region  $R < 8$  kpc and  $|z| < 4$  kpc. The total DFA is the sum of  $C_n F_n$ , but the actual relative contribution of component  $F_n$  to DFA is  $C_n M_{w,n}$ . In Fig. 6 we show the phase-space density of DFA. The combined projected moments (Sect. 3) of

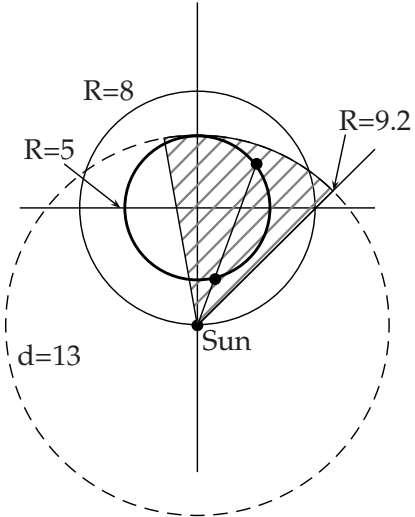


**Fig. 5.** The hatched wedge gives the part of the plane over which the distribution function is integrated to yield the moments, mimicing the observations with a horizon at 13 kpc (dashed circle  $d=13$  kpc, see Sect. 3.3). The galactic Centre is at the intersection of the straight lines. Evidently, not all galactic radii in the observed region are sampled equally well. Radii  $< 5$  kpc are sampled optimally, with two intersections at any longitude (or four for  $< 1.4$  kpc). The largest radius that is sampled is 9.2 kpc.

**Table 4.** The input library. Explanation see Sect. 3.3.

Family	$\alpha$	$\beta$	$\gamma$	$z_0$	$i_s$	$N_c$
<b>F1</b>	5, 10, 20	0, 1, 2			0, -1, 1	27
<b>F2</b>	2, 4, 8, 10	1, 2	2, 6	1, 5	-1	32

**Table 5.** The components (in order of choice by QP from Table 4) of the best-fit distribution function DFA (Sect. 4) for a horizon at 13 kpc.  $C$  gives the coefficient of the component,  $M_w$  its mass within a fixed cylinder (see Sect. 4).

Family	$\alpha$	$\beta$	$\gamma$	$z_0$	$i_s$	$C$	$M_w$
<b>F2</b>	2	2	6	1	-1	1.94E4	3.35E-2
<b>F1</b>	10	0			0	3.52E2	5.69E-1
<b>F1</b>	20	1			-1	1.54E6	2.89E-5
<b>F1</b>	20	0			0	5.92E3	9.69E-3
<b>F1</b>	5	0			0	1.43E1	1.24E+1

DFA and of the data are shown in Fig. 7 and the true projected moments (as used in the fit) in Fig. A1 (Appendix A). At the inclusion of the fifth component, the value of  $D$  (Eq. 2) has converged to within 2%, to 22% of the initial value. As explained in Sect. 3.3, we did not allow negative coefficients for the components in the model distribution function. We tested that the outcome (Table 5) is not dependent upon this; exactly the same results are obtained when negative coefficients are allowed. The small-scale (non-axisymmetric) features are, correctly, mostly neglected by QP. Apart from this, the main discrepancies between data and model are seen in the scaleheight (Fig. 7c,k), the central dispersion (Fig. 7g,h) and the vertical rotation profile at  $|\ell| \sim 8^\circ$  (Fig. 7f).

The underlying reason is the same for all these discrepancies: the dispersion is too high to be explained by a 2I model that fits the other moments. The line of sight to the galactic Centre is parallel to the radial direction, so the observed central dispersion  $\sigma_0$  depends on the radial dispersion  $\sigma_R$  only. Since the scaleheight  $h_z \propto \sigma_z^2$  and in 2I distributions  $\sigma_R \equiv \sigma_z$ , a component that increases  $\sigma_0$  will increase inevitably, via  $\sigma_R$  and  $\sigma_z$ , the scaleheight at  $\ell = 0^\circ$ . The bad reproduction of the vertical kinematic profiles arises because components that give cylindrical rotation (mainly F2) have low dispersion. Components that give vertically-constant dispersion profiles (mainly F1), as observed

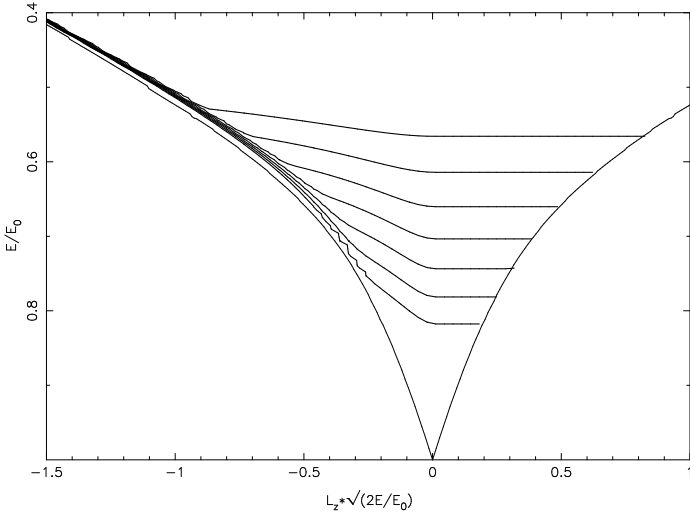


**Fig. 6.** The phase-space density as function of  $E, L_z$  (see Fig. 4) for DFA, the best-fit two-integral model. The logarithmic contours range from 1 (top) to  $10^5$  (bottom, arbitrary units), so the highest phase-space density is at  $(E, L_z) = (0.0, 1.0)$ : the central region of the Galaxy. Comparing to Fig. 4; one can clearly discern a thin disk (closely-spaced contours at negative angular momentum) and an isotropic component (horizontal contours).

for  $|\ell| > 15^\circ$ , do not have cylindrical rotation. Note that the flatness, high central dispersion and cylindrical rotation are all signs of the barred central Galaxy (eg. Kormendy 1993).

For oversmoothed data (with a kernel twice as large as the optimal kernel discussed in Sect. 3.1), the surface-density vertical profiles are fitted much better (Fig. A2c,k,l). Accordingly, the model  $\sigma_0$  is indeed higher (Fig. A2g,h) and the model rotation is more cylindrical (Fig. A2f). The fit to the dispersion is better as well, because the central dispersion is no longer so sharply peaked.

In Fig. A3 we present the model derived for the data smoothed with elongated kernels (see Sect. 3.1). The central scaleheight is now very small and the vertical surface-density profile is only fitted above  $|b| = 1^\circ$ . Therefore, the central dispersion could be fitted well; it is also lower than in the standard-smoothed data because the (central) disk contributes more, decreasing the dispersion in the plane. For  $|b| > 1^\circ$ , the minor-axis surface-density profile is modelled well at the cost of the modelled minor-axis dispersion. In Fig. A4 we show the best model using the BD2 potential (Sect. 3.2). The global rotation and dispersion are not fitted well, as expected from the discrepancy between potential and data (Fig. 2).

#### 4.1. Errors, biases and stability

To estimate the errors in the input data and in the distribution function, we applied the “bootstrap” method (Press et al. 1992). New samples were created by drawing randomly 507 stars from the data sample (consisting of 507 stars) “with replacement”. This means that the same star can appear in the sample more than once. We are allowed to do this, because the sample is virtually free of any biases (S97A, S97B). These 25 new samples were smoothed and modelled in exactly the same way as the original data. The mean of and the scatter in the results provide biases and error bars on the input gridded data as well as on the model distribution function and its moments (Fig. 7,A1): bootstrap measurements have the same distribution with respect to the original measurement as the original measurement has with respect to the “true” value. The errors arising from the gridding are small and, as expected, the data are free of bias, except for some small latitude-dependent bias (S97A, S97B; most notable in Fig. 7f). For the model, the small errors and biases indicate that the distribution function is in general well-constrained by the data and close to the “true” distribution function, *given* the limitation of being a two-integral model.

Some of the model moments are considerably biased, though (Fig. 7, A1). The mean vertical profiles in Fig. 7j,l are actually closer to the data than the best-fit model. This means that these deviations between the DFA moments and the data are not due to an intrinsic limitation of our modelling technique, but that for some reason the data cause the model to be biased, eg. via the inevitable limitations of observational sampling. One should be careful not to think

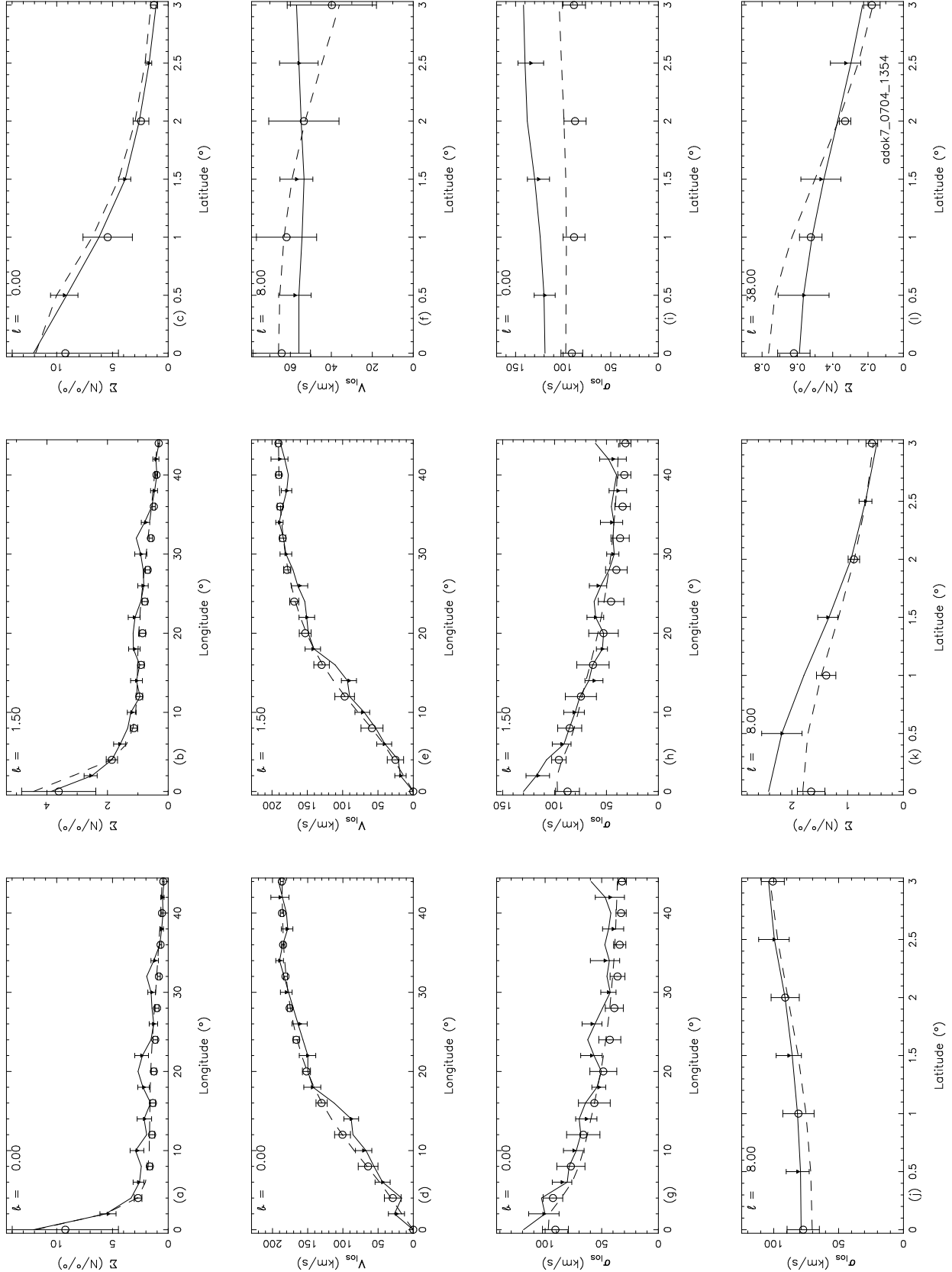


**Fig. 7.** Cuts through combined projected moments of the model distribution function DFA (dashed) and through the data (solid; see Sect. 4). The means and error bars on data (triangles) and model (circles) are found via bootstrapping (note that the curves are *not* the means, see Sect. 4.1). The data was adaptive-kernel smoothed with initial kernels of  $1^\circ \times 1^\circ \times 30 \text{ km s}^{-1}$  (see Sect. 3.1). Labels in the panels indicate for what value of latitude or longitude, respectively,

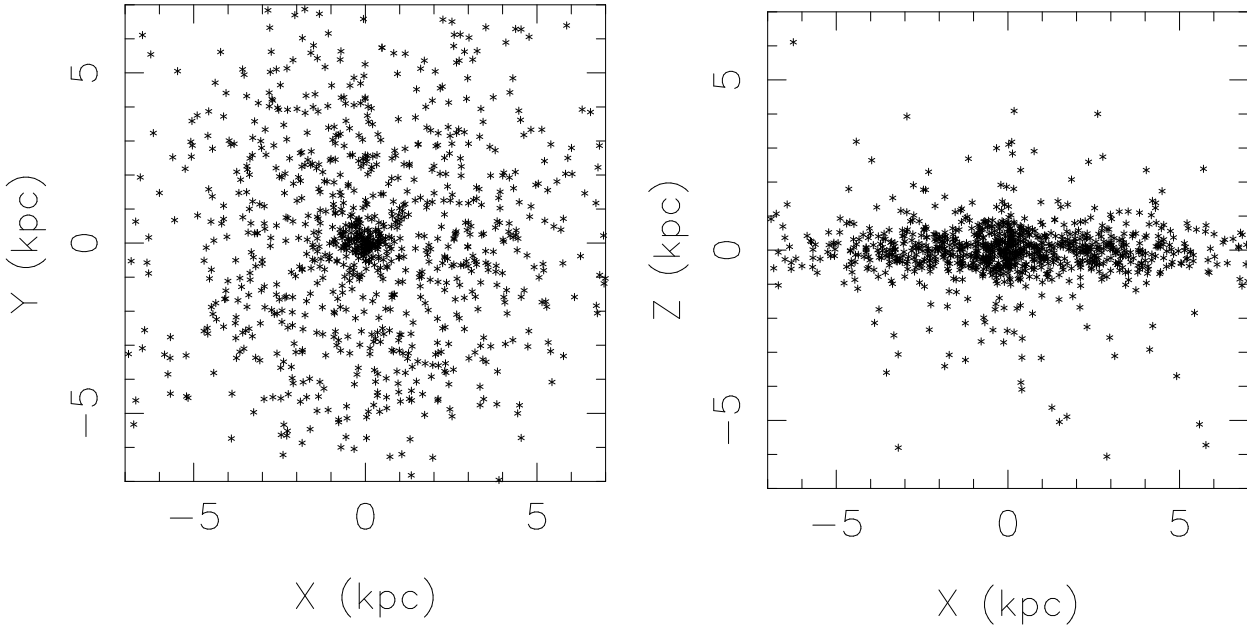


**Fig. 8.** The  $(x, y)$  and  $(x, z)$  positions for 1000 particles from the random realization of DFA.

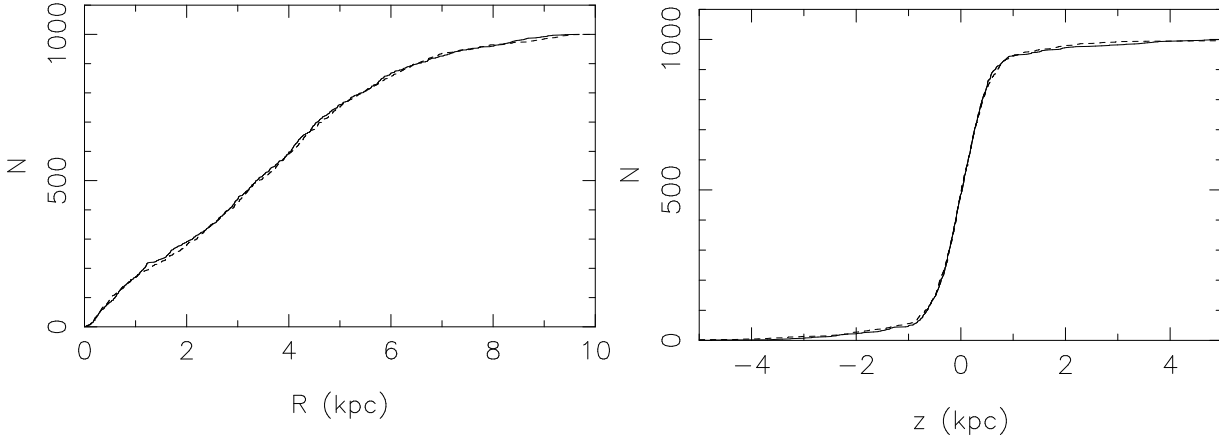


**Fig. 9.** The cumulative-number density as a function of  $R$  and of  $z$  for the initial distribution of the random realization (solid curve) and the distribution after ten galactic revolutions (dashed curve). According to the Kolmogorov–Smirnov test, the probability that initial and final distributions are the same is more than 95%.

that the “average model” is closer to the “true” distribution function than DFA is; it only means that DFA is not close to the “true” distribution function for  $|\ell| \gtrsim 35^\circ$ .

On the other hand, the biases on the model in Fig. 7c,i are away from the data. Hence the modelling technique really cannot provide good results here; one might guess using only two integrals is the inhibiting factor here. There is also a small bias ( $\sim 1\sigma$ ) away from the data on the longitude model profiles in Fig. 7a,b; this could be due to the obvious non-axisymmetric features present in the data and thus the limitation of our axisymmetric model. Similarly, the bias at larger longitudes on the model dispersion profiles (Fig. 7g,h) could be caused by the limitations of our model potential that is not quite adequate at larger radii. So, although globally the 2I model reproduces the observed moments well and with small uncertainties, it is presented with real problems by the vertical profiles at  $\ell=0^\circ$  (Fig. 7c,i), as well as by the cylindrical rotation at  $|\ell| = 8^\circ$  (Fig. 7f).

We created an  $N$ -particle realization ( $N=5000$ ) of the distribution function (see eg. van der Marel et al. 1997) and evolved it, in the global potential used in QP, to show that DFA is numerically stable, as it should be as a valid function of the integrals of motion. The realization is shown in Fig. 8, where we plot 1000 particles in the  $(x, y)$  plane and in the  $(x, z)$  plane. As criteria for stability we checked the total radial and vertical cumulative-density profiles and the total energy. To quantify the stability of the density profiles we use the Kolmogorov–Smirnov (KS) test described

**Table 6.** The components (in order of choice by QP) of the best-fit distribution function for the galactic-centre sample, integrated over a spheroid of  $0.5 \times 0.25$  kpc centered at the GC.

Family	$\alpha$	$\beta$	$\gamma$	$z_0$	$i_s$	$C$	$M_w$
<b>F2</b>	200	1	2	1	-1	$6.2E35$	$2.22E-33$
<b>F1</b>	900	2			-1	$2.9E21$	$6.14E-20$
<b>F2</b>	200	2	2	1	-1	$5.4E38$	$4.56E-36$
<b>F2</b>	900	0	2	0.1	0	$2.8E17$	$2.81E-16$
<b>F1</b>	900	3			-1	$3.1E26$	$7.98E-26$

by Press et al. (1992). The radial and vertical profiles pass the KS-test very well; the differences between the initial distribution and that after ten galactic revolutions are entirely negligible (Fig. 9, KS probability  $\gtrsim 95\%$ ). The total energy shows no variations other than of the order of the accuracy of the integration ( $10^{-6}$ ).

### 5. Third integral

The problems of the 2I fit, mentioned in Sect. 4, may be overcome by the use of three-integral (3I) models, as for these the radial and vertical dispersions do not have to be the same and therefore the radial and vertical distributions are not coupled. For axisymmetric Stäckel potentials three integrals of motion –  $E$ ,  $I_2$  ( $\equiv 0.5L_z^2$ ) and  $I_3$  – are known analytically (de Zeeuw 1985). We use QP with three types of 3I orbital components; two are derived from the components in Eq. 3,4. The third-type components are axisymmetric Abel components (Dejonghe & Laurent 1991). Using the same input data as for DFA we obtain the distribution shown in Fig. 10. The 3I distribution function comprises a few components with small, negative coefficients. The problems of the fit in DFA (Fig. 7) are largely solved; in the inner regions, the dispersion is  $20 \text{ km s}^{-1}$  higher for all latitudes and at the same time the minor-axis surface-density profile is fitted better. Also the cylindrical rotation at intermediate longitudes (Fig. 10f vs. Fig. 7f) is reproduced better; the deviation of the model rotation from the data at  $b = 3^\circ$  is only half that in the 2I model. The components of the 3I distribution function are only truly 3I inside  $\sim 4$  kpc; outside that the dependency on the third integral decreases until it disappears at the solar radius. It is well known, however, that also in the Disk a third integral is needed to describe the distribution of most populations, because the local vertical dispersion does not equal the radial dispersion (eg. Wielen 1977). We will not draw conclusions about the third integral in the Disk, as the AX2 potential does not represent properly the gravitational forces outside radii of  $\sim 5$  kpc. Clearly, in the inner regions a third integral is needed to model the observed high dispersion and small scaleheight. An upcoming counterpart to the AOSP survey covering positive longitudes (see S97A,B) will enable us to construct a proper triaxial, three-integral model. The observed positive-negative-longitude asymmetries in stellar kinematics, in combination with the known asymmetries in the stellar surface density, will be essential to do this.

### 6. The central 100 pc

In Sevenster et al. (1995; SDH) a sample of 134 stars in approximately the inner square degree of the Galaxy (Lindqvist et al. 1992) was modelled using the BD2 potential (Table 2), with an additional Plummer potential truncated at 100 pc. With the AX2 potential we obtain virtually the same results, this time without an additional Plummer potential. For the same data gridding as in SDH, over 20 nearest neighbours, there are co- and counter-rotating F2 components of similar extent (ie. similar  $\alpha$ ) and more concentrated co-rotating or fully isotropic F1 components.

It is difficult to determine the correct way to smooth this small sample and the exact results are dependent upon the smoothing. The model we give in Fig. 11 (Table 6) is obtained from the data averaged over 30 nearest neighbours. In this case no counter-rotating components are found by QP. The value of  $D$  (Eq. 2) has converged to within 1% at the inclusion of the fifth component (Table 6), but the final value of  $D$  is 60% of the initial. The latter indicates that this fit can be improved upon; there are only components with  $\alpha = 200$  and  $\alpha = 900$  in the input library so this may have been crude. The radial scale of the  $\alpha = 200$  components is roughly 200 pc; that of the  $\alpha = 900$  components 50 pc. The rotation in the inner 100 pc comes from the F1 components.

This is even more pronounced if we use only the 10 nearest neighbours to calculate the moments. In this case the observed dispersion at  $b=0^\circ$  increases from  $50 \text{ km s}^{-1}$  at  $\ell = 0^\circ$  to  $120 \text{ km s}^{-1}$  at  $\ell = 0^\circ.6$ , which is the observed value for the AOSP sample (Fig. 7). The  $\alpha = 200$  are co- and counter-rotating, respectively, as in found in other runs, mainly to fit this increasing dispersion. All rotation comes from  $\alpha = 900$  F1 components in this case.

Possibly the  $\alpha = 200$  components are connected to a part of the GC sample that forms the innermost extension of the Bulge; the kinematics, radial scale and large vertical scale ( $z_0 = 1$  kpc) fit in well with that. The counter-

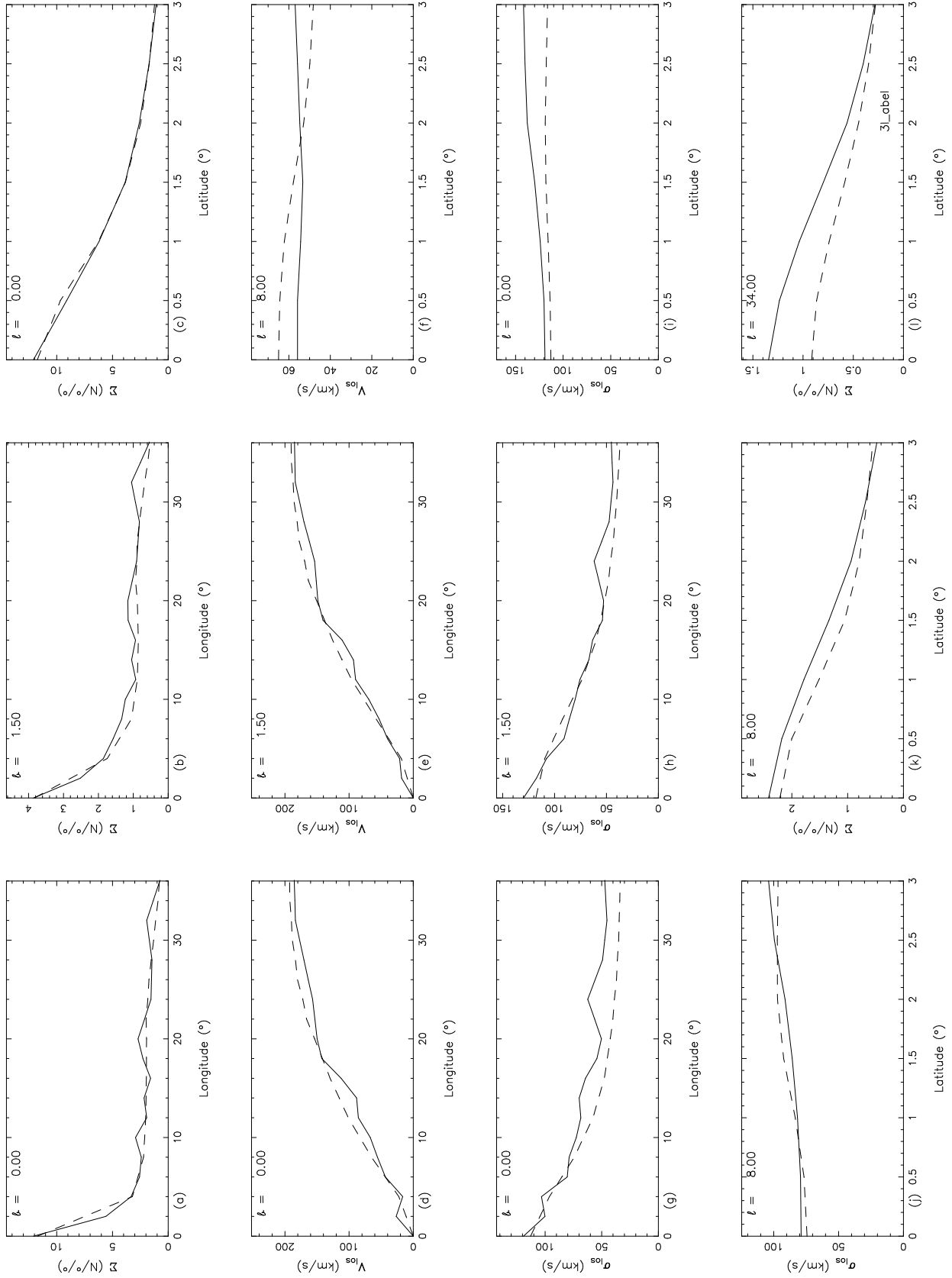
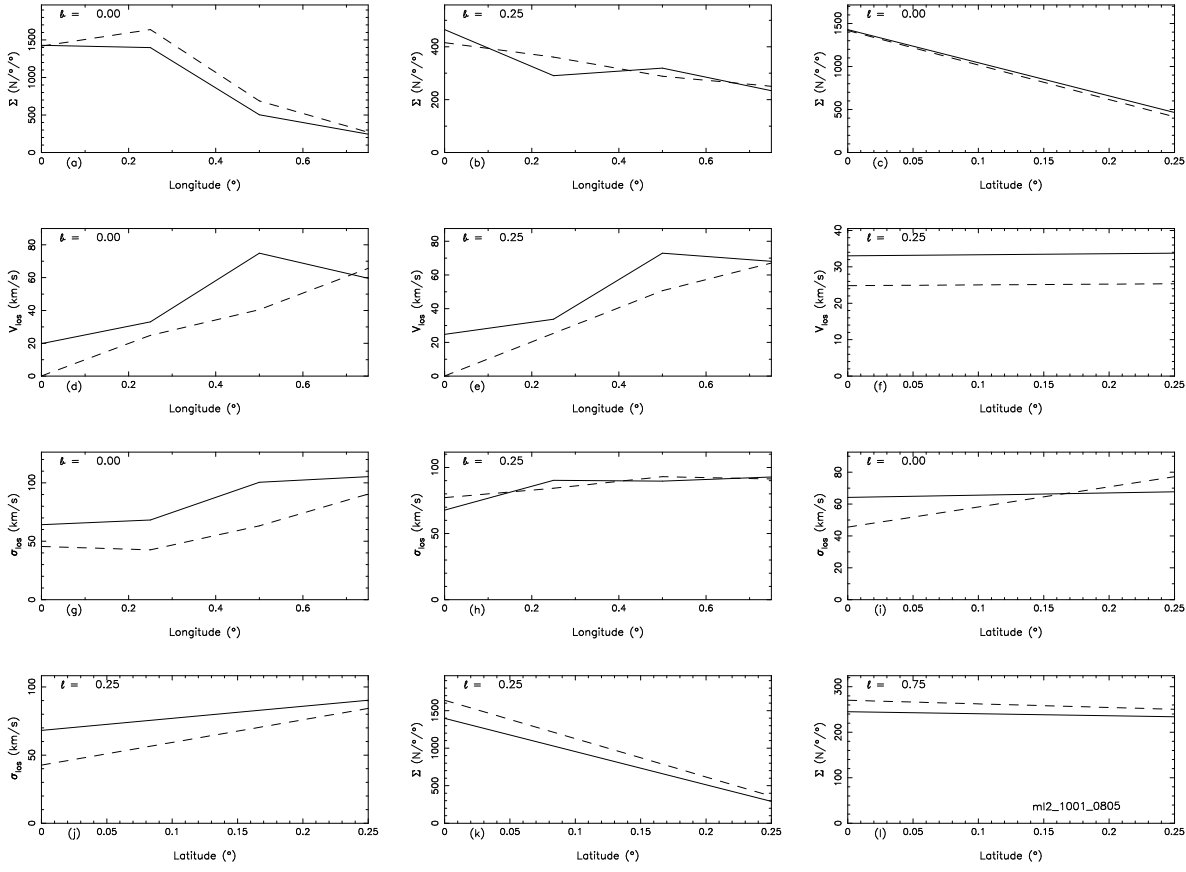


Fig. 10. As Fig. 7, for the 3I model (Sect. 5).



**Fig. 11.** The fit to the sample of galactic-centre stars (data averaged over 30 nearest neighbours; see Sect. 6). The cuts are at different longitudes and latitudes than in Fig. 7.

rotation in these components found for a range of inputs is used to increase the dispersion artificially; possibly the central concentration of the potential is not fully adequate; or a third integral, that reproduced the large AOSP central dispersion, is needed also in this model. The  $\alpha = 900$  components may form the true GC sample (SDH; Sjouwerman et al. 1998a,b; Sevenster 1999), judging from their high rotation and small radial and vertical scales. These components are probably formed mainly by high-outflow sources.

## 7. Discussion

### 7.1. Density

For the 2I as well as the 3I model, the scalelength and scaleheight at  $R = 6$  kpc are 2.5 kpc and 200–250 pc, respectively. At  $R = 0$  kpc, they are 200–220 pc and 150 pc. These scales are very similar to those found for the same sample in an analysis of the surface density only (Sevenster 1999), except for the scalelength that is smaller but still large with respect to most determinations of the scalelength (see Sackett 1997), although Binney, Gerhard & Spergel (1997) also find a scalelength of 2.5 kpc from fitting COBE data.

### 7.2. Orbits

The fractions of co-rotating and of eccentric orbits, respectively, can be defined by the following formulae :

$$F_{\text{corot}} \equiv \int_{-L_{\max}}^0 f(E, L_z) dL_z / \int_{-L_{\max}}^{+L_{\max}} f(E, L_z) dL_z \quad 5$$

$$F_{\text{ecc}} \equiv \int_{-0.5L_{\max}}^{+0.5L_{\max}} f(E, L_z) dL_z / \int_{-L_{\max}}^{+L_{\max}} f(E, L_z) dL_z \quad 6$$

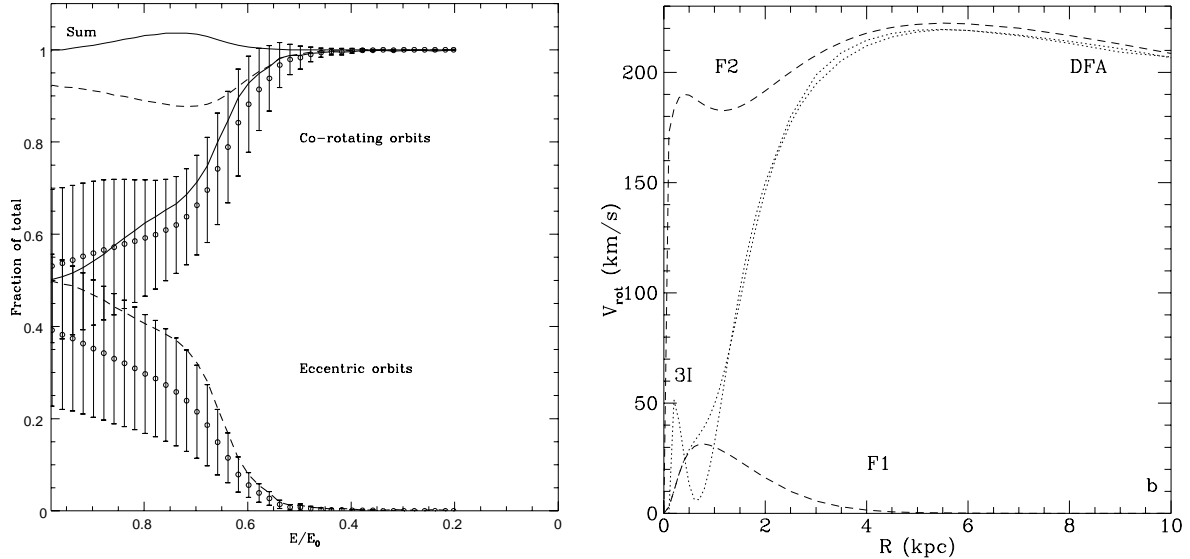


**Fig. 12.** (a) The fractions of the phase-space density on co-rotating orbits (Eq. 5, thick solid curve) and on eccentric orbits (Eq. 6, thick dashed curve). The sum of the two (thin solid curve) equals 1 only if the distribution is fully isotropic, fully co-rotating or contains only eccentric orbits. The biases (points) and errorbars are obtained via bootstrapping (Fig. 7, Sect. 4); the thin dashed curve gives the sum of the two bootstrap-means. DFA is fully isotropic in the centre ( $E = 1$ ), but the bias indicates that the AOSP sample is not. (b) The mean rotation for DFA and the 3I model, as well as for the F1 and F2 components of DFA separately, is shown as a function of radius.

where  $L_{\max}$  is the absolute value of the angular momentum of a circular orbit with energy  $E$ . In Fig. 12a these fractions are shown for DFA. In the centre ( $E/E_0 > 0.95$ , which coincides for circular orbits with  $R_{\text{cir}} < 160$  pc, for radial orbits with  $R_{\text{rad}} < 230$  pc, Fig. 4) the distribution function is isotropic to within 1%. For  $E/E_0 < 0.5$  ( $R_{\text{cir}} > 2.5$  kpc,  $R_{\text{rad}} > 4$  kpc) more than 99% of the mass is on almost-circular, co-rotating orbits. The biases and errorbars indicate that the distribution function at high binding energies is not very well-constrained. This can be seen in the moments only for the surface density, for which the errorbars near the galactic Centre are large (Fig. 7a,b,c).

There is considerable bias on the fraction of DFA on eccentric orbits, which means that this fraction is not close to the “true” fraction of eccentric orbits in the central Galaxy. The fraction of co-rotating orbits is less biased and always larger than 50% (in the mean), so there is no significant net counter rotation in the AOSP sample.

There is a turn-over in the energy distributions in Fig. 12a at  $E/E_0 \sim 0.7$  ( $R_{\text{cir}} = 840$  pc,  $R_{\text{rad}} = 1.4$  kpc) and the fractions of eccentric orbits and of counter-rotating orbits decrease quickly outside this radius. Around  $R = 800$  pc, the rotation curve of the F1 component (Fig. 12b) reaches its maximum ( $31.5 \text{ km s}^{-1}$ ). The rotation is continued fairly smoothly by the F2 component, though. A disk and a bulge-like regime can be identified in energy, but not so clearly in radius, although a mild transition can be seen at a radius 2.5 kpc (Fig. 9). There is an “isotropic-rotator” regime inside  $\sim 1$  kpc outside which the disk starts. Between 1 kpc and 4 kpc the isotropic components contribute to a non-negligible fraction of mass on eccentric and counter-rotating orbits. The rotation is almost linear out to 2.5 kpc, outside 4 kpc the regime is purely disk. This is in agreement with arguments that barred bulges do not extend beyond their co-rotation radius (eg. Contopoulos & Grosbøl 1986; Elmegreen & Elmegreen 1985), which in the Galaxy is at 4 to 5 kpc.

### 7.3. Dispersions

The dispersions that derive from DFA are obviously biased by the fact that  $\sigma_R \equiv \sigma_z$ . At the solar radius, DFA yields  $(\sigma_R, \sigma_\phi, \sigma_z) = (11 \text{ km s}^{-1}, 22 \text{ km s}^{-1}, 11 \text{ km s}^{-1})$  so  $\sigma_p \equiv \sqrt{(\sigma_\phi^2 + \sigma_R^2)} = 25 \text{ km s}^{-1}$  (Fig. 13a). This  $\sigma_p$  agrees with a population of  $\sim 1.5$  Gyr for which the observed full velocity ellipsoid is  $(19 \text{ km s}^{-1}, 15 \text{ km s}^{-1}, 10 \text{ km s}^{-1})$  (Wielen 1977). So  $\sigma_\phi$  is forced to reproduce most of  $\sigma_{\text{los}}$  as  $\sigma_R$  cannot be larger than  $\sigma_z$ , that in turn is limited by the scaleheight. In the 3I model, the local dispersions are all  $13 \text{ km s}^{-1}$ . For young stars ( $< 0.5$  Gyr), the three dispersions are observed to be almost equal, but have a much lower value. The 3I dispersions yield  $\sigma_p = 18 \text{ km s}^{-1}$ , equivalent

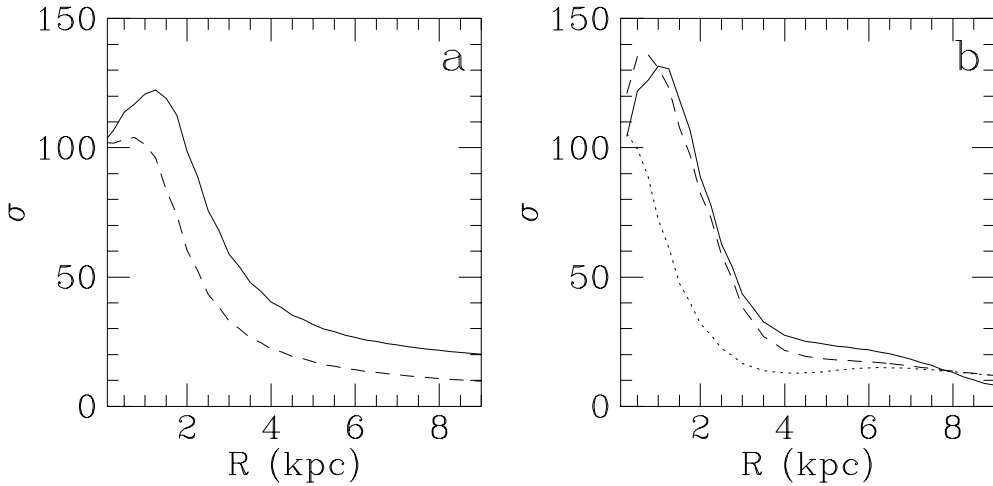


**Fig. 13.** The radial (dashed), the azimuthal (solid) and the vertical (dotted) dispersions in  $\text{km s}^{-1}$  at  $z = 0$  for DFA (a) and the 3I model (b) as a function of radius. For DFA the vertical dispersion equals the radial.

**Table 7.** The components (in order of choice by QP from Table 4) of the best-fit model to the high-outflow sources (horizon 13 kpc).

Family	$\alpha$	$\beta$	$\gamma$	$z_0$	$i_s$	$C$	$M_w$
<b>F2</b>	10	1	6	1	-1	$7.1E5$	$1.07E-5$
<b>F2</b>	2	2	6	1	-1	$5.2E3$	$3.35E-2$
<b>F1</b>	20	0			0	$2.3E3$	$9.70E-3$
<b>F1</b>	5	2			1	$5.8E2$	$2.58E-1$
<b>F1</b>	20	1			-1	$2.8E5$	$2.89E-5$

to observations of stars of  $\sim 1$  Gyr, for which the full velocity ellipsoid is  $(14 \text{ km s}^{-1}, 11 \text{ km s}^{-1}, 8 \text{ km s}^{-1})$  (Wielen 1977). Despite the decoupling from  $\sigma_z$ ,  $\sigma_R$  is still not larger than  $\sigma_\phi$ . As we already noted in Sect. 5, the 3I model does not contain 3I components at radii larger than  $\sim 4$  kpc. Although individually  $\sigma_R$  and  $\sigma_\phi$  do not match observations, the dispersion in the plane  $\sigma_p$  has the value expected for a population of the average age of the OH/IR stars in the Disk ( $\sim 1.5$  Gyr, Sevenster 1999). Keeping in mind that our model potential is not fully adequate at radii larger than 5 kpc, the “deviant” model-dispersion ratios may indicate that a significant number of OH/IR stars is not on epicyclic orbits.

A well-observed dispersion is the line-of-sight dispersion toward Baade’s window ( $\ell = 1^\circ, b = -4^\circ$ ) of  $113^{+6}_{-5} \text{ km s}^{-1}$  (Sharples et al. 1990). DFA yields  $107 \text{ km s}^{-1}$  and the 3I model  $113 \text{ km s}^{-1}$ , hence the observed dispersion, even at the higher latitude of Baade’s window, is matched somewhat better by the 3I model. The proper-motion dispersions toward Baade’s window are  $(\sigma_\ell, \sigma_b) = (3.2 \pm 0.1 \text{ mas yr}^{-1}, 2.8 \pm 0.1 \text{ mas yr}^{-1})$  (Spaenhauer et al. 1992). DFA and the 3I model yield  $(1.6, 1.5)$  and  $(3.5, 2.4)$ , respectively (taking the detectability of sources inversely proportional to the distance squared and integrating out to 8 kpc).

#### 7.4. Disk versus Bulge

Imagine that the total distribution function, DFA, indeed fully describes the stellar dynamics of the Galaxy. Each OH/IR star can be thought of as a random realization of DFA – more specifically, as drawn from one of the DFA components. The probability, then, that a star S is drawn from, say, component DFA1, is the conditional probability  $(S \in \text{DFA1} | S \in \text{DFA})$ . This, according to Bayes’ rule, is proportional to the density of the component at the position of S. Hence, the component with the highest density, integrated over the unmeasured coordinates, at the position of a star, is most likely to have “generated” that star.

In Fig. 14 we show this by plotting for each component of Table 5 the longitude–latitude diagram and longitude–velocity diagram of the stars for which this component gives greatest probability. Although one should be careful to interpret the components of the distribution function exactly as physical components of the Galaxy, it is clear that

**Table 8.** The components (in order of choice by QP from Table 4) of the best-fit model to the low-outflow sources (horizon 11 kpc).

Family	$\alpha$	$\beta$	$\gamma$	$z_0$	$i_s$	$C$	$M_w$
<b>F1</b>	5	1			-1	1.4E1	6.66E-1
<b>F2</b>	2	2	6	1	-1	2.9E3	3.35E-2
<b>F1</b>	20	1			-1	7.2E5	2.89E-5
<b>F1</b>	10	0			0	3.7E2	5.69E-1
<b>F2</b>	2	2	2	1	-1	1.1E3	4.66E-3

the first component DFA1 forms the main galactic Disk and DFA2–4 are connected with a slowly rotating isotropic bulge. The role of DFA5 is difficult to assess. The fraction of stars with longitudes below  $-20^\circ$  that connect to DFA5 is 25%. However, the mass fraction of this component is of the order of 2% for radii larger than 2.5 kpc (Fig. 12). The Disk stars connected to DFA5 are probably mainly those that make up the local features that are not fitted by DFA (Fig. A1). As those stars have rather deviant velocities, they fit in best with DFA5, because it has very high velocity dispersion ( $\sim 100 \text{ km s}^{-1}$ ). This does *not* mean that those stars instigated the inclusion of DFA5 in DFA, after all they are not properly represented by the fit. DFA5 may represent the tail of the Bulge, that apparently protrudes to  $R \sim 4$  kpc (cf. Fig. 12a). Indeed the stars connected to DFA5 have the lowest total probability to be connected to DFA, supporting the idea that they were not really fitted very well. The most probable component is DFA4, followed by DFA1. The star with the lowest probability to come from DFA is the one in the extreme lower right corner of Fig. 14e,f,k,l.

We tentatively connect the F1 components to the Bulge and the F2 component to the Disk. As DFA1 is well constrained by stars in regions where only the Disk is contributing, we may conclude that also at lower longitudes it represents the (foreground) Disk, as is supported by Fig. 14a,g. This means that 50% of the AOSP sample is identified with the Disk and that the fraction of Disk stars at  $|\ell| < 5^\circ$  is 20%.

### 7.5. Young versus Old

In Fig. 14 different symbols are used for high-outflow, low-outflow and single-peaked sources, respectively. OH/IR stars with high outflow velocities are in general younger than those with low outflow velocities (see Sevenster 1999 and references therein). The single-peaked sources can be either (very) young or (very) old; we will not include them in this discussion. All F1 components of DFA have more low-outflow- than high-outflow sources (4:3) connected to them. For the F2 component this is exactly the other way around, as expected from the fact that it connects to Disk sources mainly. We can assess further the age-dependence of the distribution function by modelling the two groups, separated in outflow velocity at  $14 \text{ km s}^{-1}$  (excluding single-peaked sources), individually, with the same potential and library we used to obtain DFA. The results are given in Table 7 and Table 8, respectively.

The main disk (DFA1) and the rotating-bulge component DFA3 return for both the low-outflow- and the high-outflow sources. DFA4 returns for the high-outflow sources only and DFA2 for the low-outflow sources. These components are the main Bulge components, a younger and an older (more extended), respectively, forming the “isotropic rotator” together with DFA3 (Sect. 7.2). The high-outflow sources have an extra F2 component with the same vertical extent as the main DFA disk, but more centrally concentrated and less strongly rotating. This may be the youngest part of the Bulge that is not massive enough to be seen in DFA. The low-outflow sources have an extra F2 component that has the same radial extent and rotation ( $\beta$ ) as the main DFA disk, but is less concentrated toward the plane ( $h_z=300 \text{ pc}$ ). This may be the older Disk, heated from the flatter Disk. Again it is not massive enough to appear in DFA.

In Fig. A5&A6 we show the fits of DFA and the distribution function of Table 8, respectively, to a sample of OH/IR stars that reaches higher latitudes than the AOSP sample but is incomplete in the plane ( $|b| < 3^\circ$ ; te Lintel Hekkert et al. 1991). The coefficients for the components of DFA and Table 8 are redetermined for this sample. We use the horizon that optimizes the fit to the surface density (13 kpc). Clearly, a thicker disk component such as seen in the low-outflow sources is essential to explain the still cylindrical rotation in the Lintel sample; in fact the coefficient for the F2 component with  $\gamma = 6$  is zero for the fit in Fig. A6 (as this flat component would be severely undersampled by the Lintel sample). At the higher latitudes of the Lintel sample the stars are on average older, like the low-outflow AOSP sources, and these older stars apparently need a thicker disk component, primarily to describe their kinematics. The transition between the Disk and the Bulge (Fig. 12), at least at higher latitudes, is more continuous than suggested by DFA (Fig. A5e vs. Fig. A6e; see discussion in Sect. 7.2).

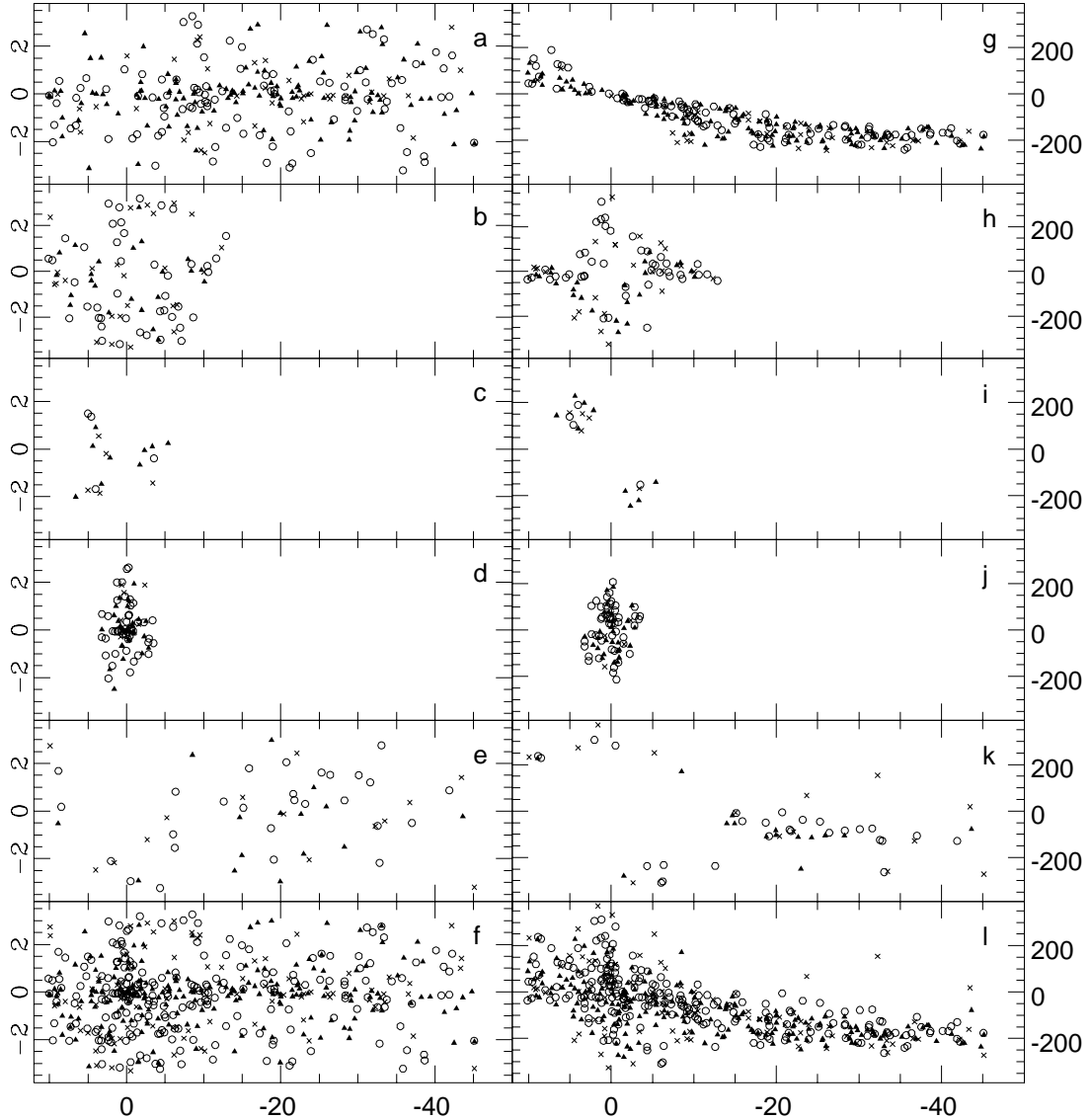


**Fig. 14.** This figure shows, for each component (from the top down in the order of Table 5; in the bottom panel for DFA in total), the longitude-latitude diagram (left) and longitude-velocity diagram (right) of the stars “associated” with it. The different symbols indicate high-outflow (triangles), low-outflow (circles) and single-peaked (crosses) OH/IR stars. For further explanation see Sect. 7.4.

In summary, it seems that there are no distinct dynamical components such as a Bulge or a thick Disk. In fact, the young Bulge has a part that in vertical extent is very similar to the Disk, in radial extent to the more isotropic older Bulge and intermediate in its degree of rotation. The older Disk is very similar in radial extent and rotation to the younger disk, only a little thicker and as such connecting even more smoothly to the Bulge. We do not sample the very old Bulge ( $\gtrsim 10$  Gyr), that may be the inner halo or “ $r^{-3.5}$  spheroid” and was found to be dynamically different from the younger “nuclear Bulge” by Rich(1990).

The connection we find between Bulge and Disk, especially their similar vertical extent for the younger stars, is in agreement with the notion that the Bulge is triaxial and that this Bar formed via disk instability (see Sevenster 1999). Of course, we have already seen several signatures of the existence of the Bar, in the need for a third integral to explain the dynamics in the central degrees and the the cylindrical rotation (see discussion in Kormendy 1993).

Note that in this case, the fraction of foreground disk stars we estimated earlier for the central  $10^\circ$  (20%) may be too high, as part of the disk-like Bar stars would probably be modelled by DFA1 as Disk stars.

## 8. Conclusions

Using a simple, axisymmetric potential we construct a stable two-integral distribution function (DFA) that gives a very good global fit, in the first three projected moments, to our “AOSP” sample of OH/IR stars in the plane. Some detailed discrepancies between the model DFA and the data indicate that the distribution of OH/IR stars is influenced by the barred potential in the inner regions of the Galaxy. A three-integral model improves the fit for the inner regions considerably, even with the same axisymmetric potential. Durand et al. (1996) also concluded there is a need for a third integral, from similar work on distribution functions, using planetary nebulae.

The energies of stars in the plane seem to separate into a bulge-like and a disk regime at  $E/E_0 \sim 0.7$ . This separation, as seen in DFA, is too distinct, however, when compared to the kinematics of an OH/IR star sample at higher latitudes. We conclude there is no evidence for discrete large components in the inner plane. On the contrary, models of several subsamples of younger and older OH/IR stars suggest that the Disk and the Bulge are very similar. We confirm the result of Sevenster et al. (1995) that a sample of galactic-centre OH/IR stars may consist of the inner-most part of the Bulge plus an extra component. The latter is the only truly distinct dynamical component in the inner galactic plane.

*Acknowledgements.* We thank Tim de Zeeuw and Agris Kalnajs for many useful suggestions and Prasenjit Saha for advice about statistical issues.

## References

Allen D., Hyland A., Jones T., 1983, MNRAS 204, 1145  
 Batsleer P., Dejonghe H., 1994, A&A 287, 43  
 Batsleer P., Dejonghe H., 1995, A&A 294, 693  
 Binney J., Dehnen W., 1997, MNRAS 287, 15  
 Binney J., Gerhard O., Spergel D., 1997, MNRAS 288, 365  
 Burton W., Gordon 1978, A&A 63, 7  
 Caldwell J., Coulson I., 1989, In: Blitz, Lockman (eds.) *The outer Galaxy*. Springer, p. 68  
 Contopoulos G., Grosbol P., 1986, A&A 155, 11  
 Creze M., Chereul E., Bienayme O., Pichon C., 1998, A&A 329, 920  
 Dejonghe H., de Zeeuw P.T., 1988, ApJ 333, 90  
 Dejonghe H., 1989, ApJ 343, 113  
 Dejonghe H., Laurent D., 1991, MNRAS 252, 606  
 Durand S., Dejonghe H., Acker A., 1996, A&A 310, 97  
 Dwek E. et al. 1995, ApJ 445, 716  
 de Zeeuw P.T., 1985, MNRAS 216, 273  
 Elmegreen B., Elmegreen D., 1985, ApJ 288, 438  
 Evans D., Irwin M., 1995, MNRAS 277, 820  
 Feast M., Whitelock P., 1997, MNRAS 291, 683  
 Frogel J., 1988, ARA&A 26, 51  
 Fux R., 1997, A&A 327, 983  
 Hanson R., 1987, AJ 94, 409  
 Honma M., Sofue Y., 1997, PASJ 49 453  
 Kerr F., Lynden-Bell D., 1986, MNRAS 221, 1023  
 Kochanek C., 1996, ApJ 457, 228  
 Kormendy J., 1993, In: Dejonghe H., Habing H.J. (eds.) *Proc. IAU Symp. 153, Galactic Bulges*. Reidel, Dordrecht, p. 209  
 Kuijken K., Gilmore G., 1989a, MNRAS 239, 605  
 Kuijken K., Gilmore G., 1989b, MNRAS 239, 651  
 Lindqvist M., Winnberg A., Habing H., Matthews H., 1992, A&AS 92, 43  
 Merrifield M., 1992, AJ 103, 1552  
 Merritt D., Tremblay B., 1994, AJ 108, 514  
 Oort J.H., 1965, In: Blaauw A., Schmidt M. (eds.) *Galactic Structure*. Chicago, p. 455  
 Pont P., Mayor M., Burki G., 1994, A&A 285, 415  
 Press W., Teukolsky S., Vetterling W., Flannery B., 1992, “Numerical Recipes”  
 Rich M., 1990, ApJ 362, 604  
 Rohlfs K., Boehme R., Chini R., Wink J., 1986, A&A 158, 181  
 Sackett P., 1997, ApJ 483, 103  
 Schechter P., Aaronson M., Cook K., Blanco V., 1989, In: Blitz, Lockman (eds.) *The outer Galaxy*. Springer, p. 31  
 Schwarzschild M., 1979, ApJ 232, 236  
 Sevenster M.N., Dejonghe H., Habing H.J., 1995, A&A 299, 689 (SDH)  
 Sevenster M.N., Chapman J.M., Habing H.J., Killeen N.E.B., Lindqvist M., 1997a, A&AS 122, 79 (S97A)

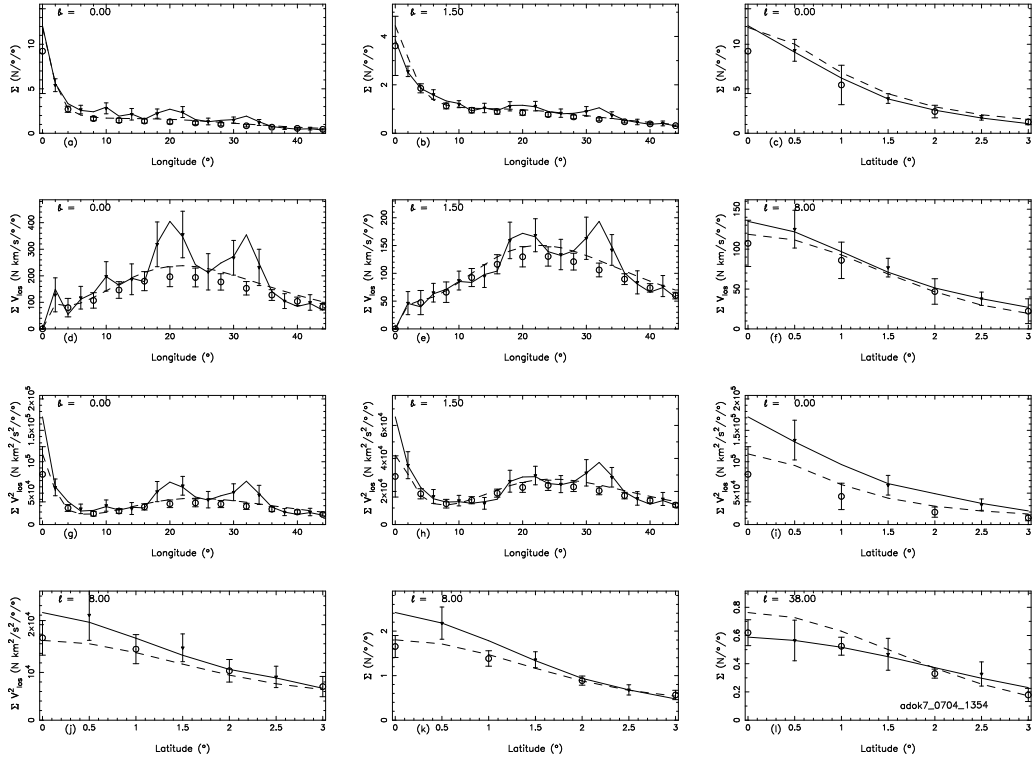


Fig. A1 As Fig. 7, for true projected moments (see Sect. 3).

Sevenster M.N., Chapman J.M., Habing H.J., Killeen N.E.B., Lindqvist M., 1997b, A&AS 124, 509 (S97B)

Sevenster M.N., 1999, MNRAS 310, 629

Sharples R., Walker A., Cropper M., 1990, MNRAS 246, 54

Sjouwerman L., Langevelde H. van, Winnberg A., Habing H., 1998a, A&AS 128, 35

Sjouwerman L., Habing H., Lindqvist M., Langevelde H. van, Winnberg A., 1998b, in Falcke et al.(eds), GC Workshop 1998, ASP

Spaenhauer A., Jones B., Whitford A., 1992, AJ 103, 297

te Lintel Hekkert P., Caswell J., Habing H.J., Haynes R., Wiertz W., 1991, A&AS 90, 327

van der Marel R., Sigurdsson S., Hernqvist L., 1997, ApJ 487, 153

Wielen R. 1977, A&A 60, 263

Zhao H.S., 1996, MNRAS 283, 149

## Appendix A Figures for derived models

In this appendix we show the figures of the cuts in longitude and latitude for a variety of models discussed in the main text.

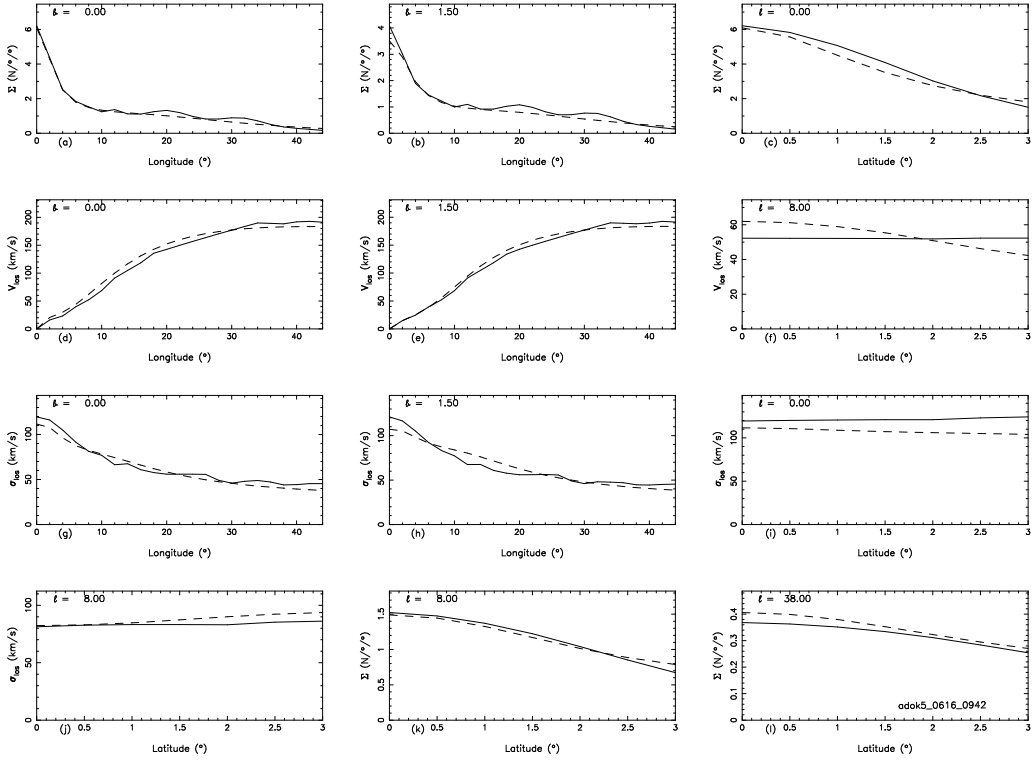


**Fig. A2** As Fig. 7, for best-fit distribution function for data smoothed with spatial initial kernel of  $2^\circ$  (same library as DFA; Table 4).

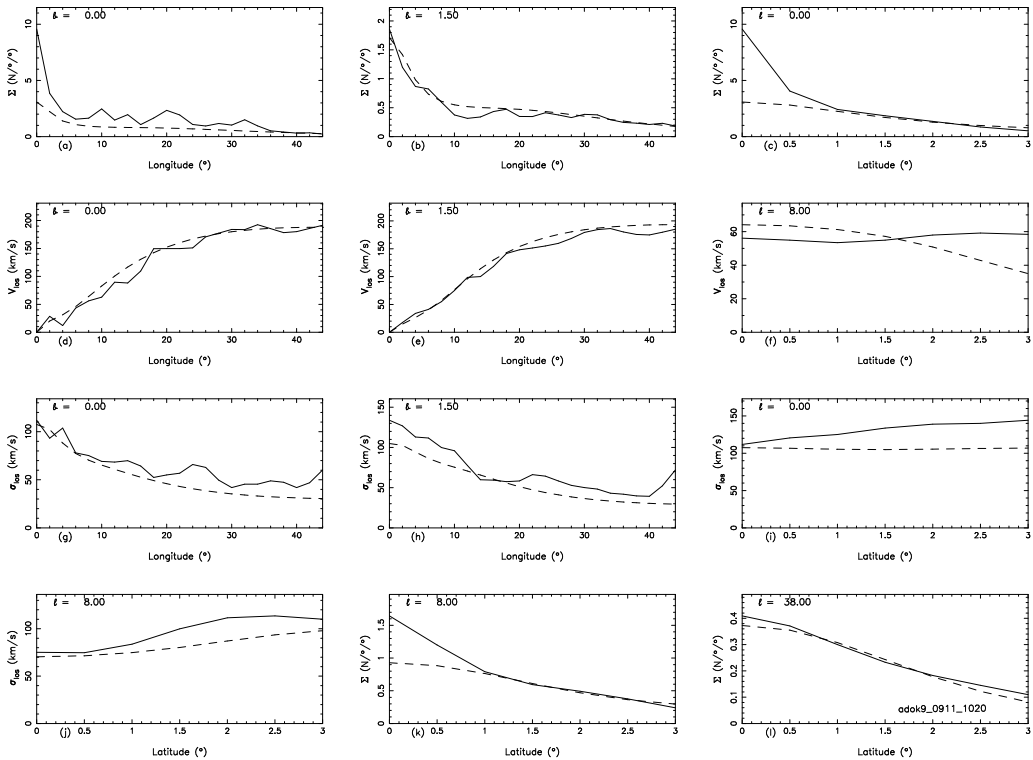


**Fig. A3** As Fig. 7, for best-fit distribution function for data smoothed with spatial initial kernel of  $1^\circ:0.5^\circ$  (same library as DFA; Table 4).

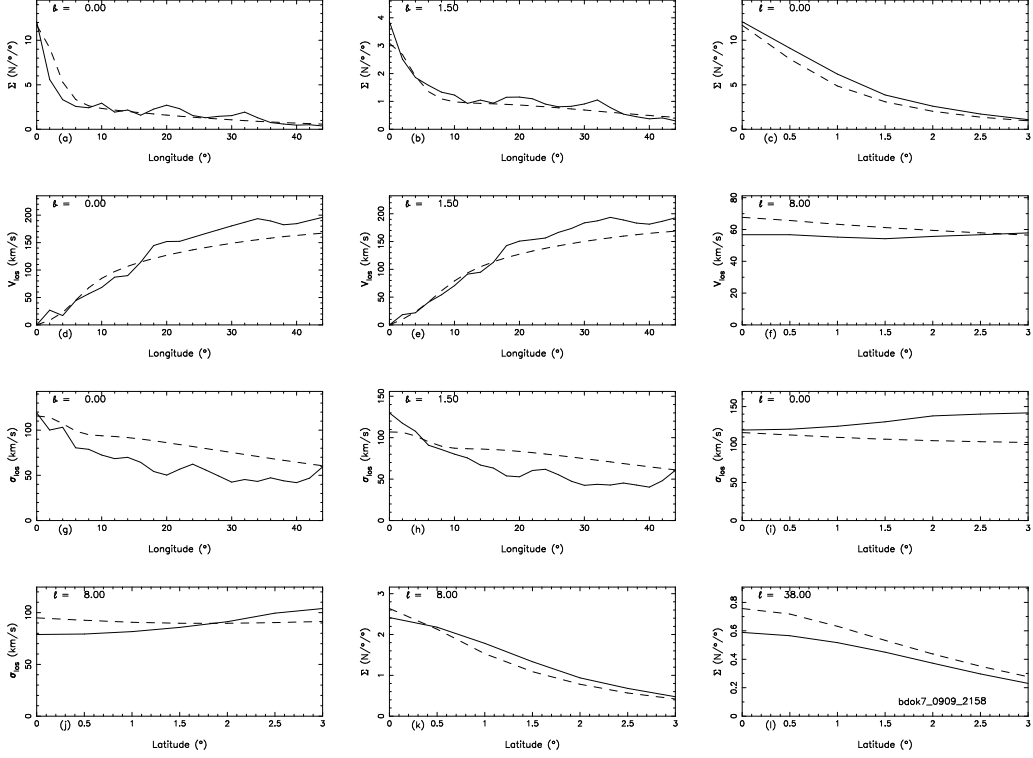


**Fig. A4** As Fig. 7, for best-fit distribution function with BD2 potential (Table 2) and the combined component library (258 components, Sect. 3.3).

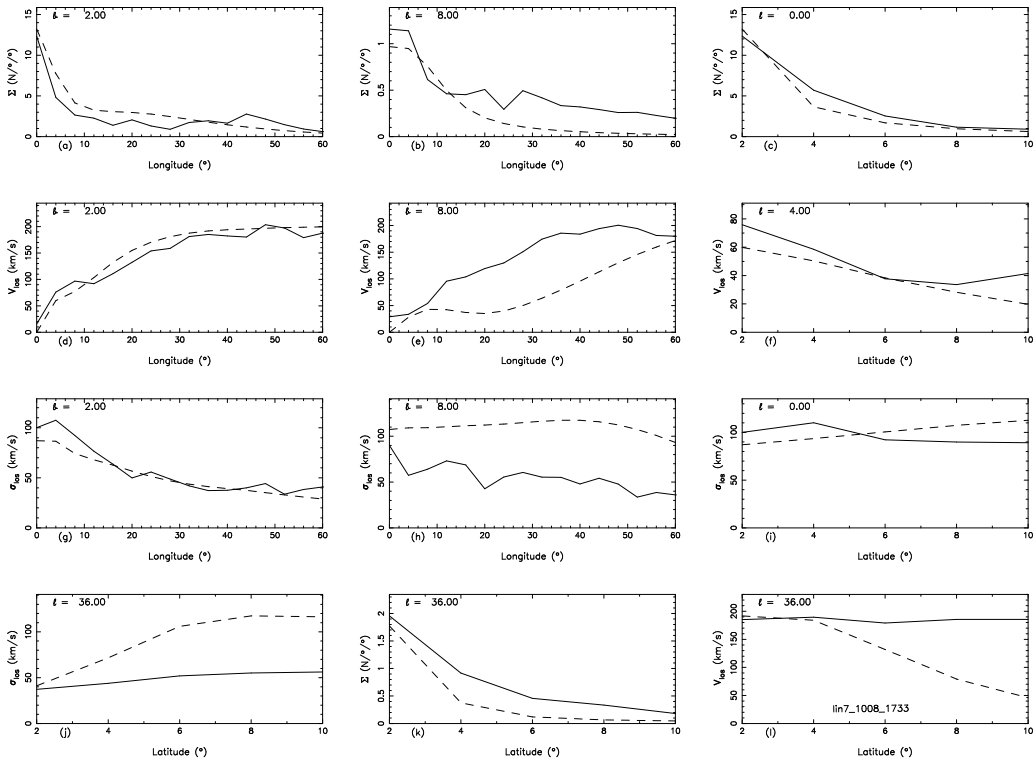


**Fig. A5** Fit of DFA (Table 5, different coefficients) to the Lintel sample. The horizon is at 13 kpc.

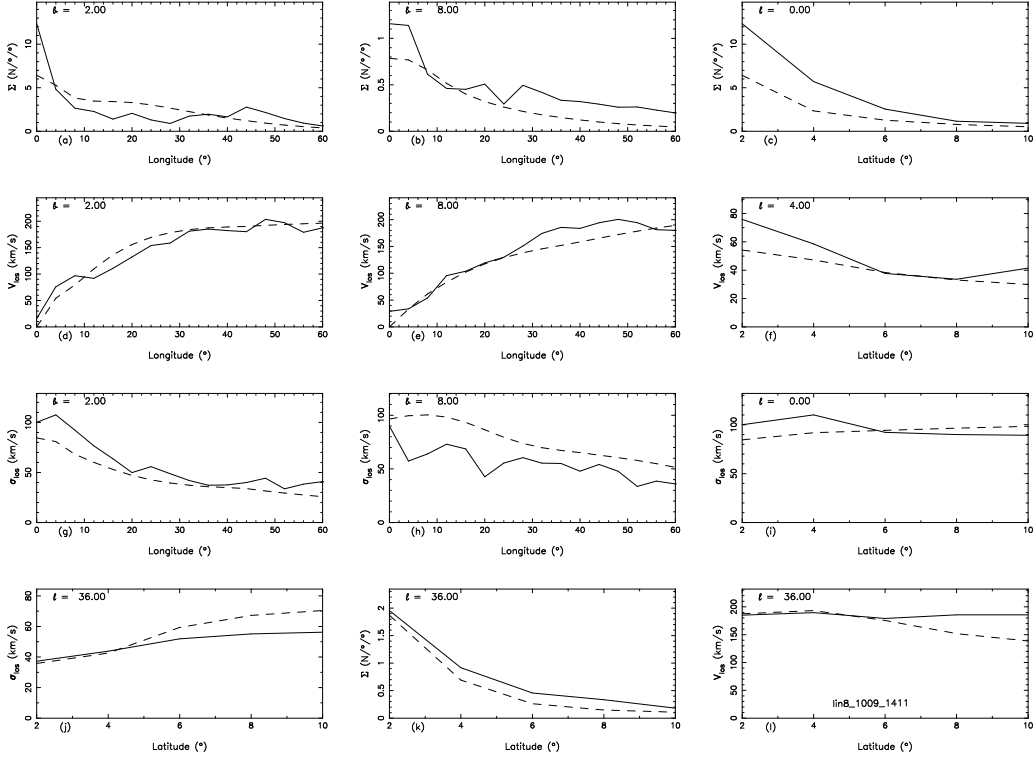


**Fig. A6** Fit of the low-outflow-AOSP distribution function (Table 8, different coefficients) to the Lintel sample. The horizon is at 13 kpc.